JOURNAL OF COMPUTATIONAL PHYSICS 102, 277–296 (1992)

A Vlasov Particle Ion Zero Mass Electron Model for Plasma Simulations

F. KAZEMINEZHAD AND J. M. DAWSON

Physics Department, University of California, Los Angeles, California

J. N. LEBOEUF

Oakridge National Laboratory, Oakridge, Tennessee

AND

R. SYDORA AND D. HOLLAND

Physics Department, University of California, Los Angeles, California

Received June 6, 1990; revised November 1, 1991

We have extended a particle-MHD model of discrete fluid ions and massless fluid electrons to the fully kinetic ions and massless fluid electrons so that such important kinetic effects, e.g., the finite Larmor radius effects, are incorporated; 2D as well as 3D versions exist. As a result the model now exhibits ion Bernstein waves. We have also developed a linear theory of the model and obtained the linear dispersion relation. The dispersion relation is in excellent agreement with results from the model. Two important improvements in numerical procedures have been implemented; the first is the elimination of unphysical short wavelength disturbances by a smoothing technique; the second is the implementation of the Richardson extrapolation (extrapolation to $\Delta t = 0$) technique in the velocity difference equations. These improvements increased the range of stability of the code greatly and enabled us to use time steps which are 10 times larger. As one application, we use the model to simulate the interaction of a neutral gas and an ambient plasma and observe the generation of waves with frequencies at integral as well as half-integral ion cyclotron harmonics for all **k** in accordance with some recent experimental observations in the JET tokamak. © 1992 Academic Press, Inc.

CONTENTS

Introduction.
1. *Analytic treatment.*
2. *Numerical model and its test.*
3. *Application: Simulation of the ion cyclotron emission in the JET tokamak.* 3.1. Simulation of the neutral beam injection. 3.2. Simulation of the fusion product experiments.

Appendix A. *Derivation of the dispersion relation.*

Appendix B. *The error dependence of* $\mathbf{v}_i$ *on the time step* Δt.

INTRODUCTION

The present work is the outgrowth of earlier work on the hybrid particle–fluid modeling which were presented in previous publications [1–4]. In those articles a model which treated ions as fluid elements and electrons as a massless fluid was presented. It was shown how the two- and three-dimensional versions of that code predicted most MHD (including whistlers and ion cyclotron) waves and were in excellent agreement with linear analytic predictions.

As we tried to simulate certain phenomenon which had been observed to generate ion Bernstein modes, we observed that the model did not yield sharp peaks at the ion Bernstein harmonics.

At that point we realized we could treat the ions kinetically (as discrete particles) rather than as a fluid and we modified the code accordingly. This modification sharpened the peaks of the power spectra at the various ion cyclotron harmonics for all the wave modes. The code was then tested by comparisons of the observed dispersion relations from simulations with those predicted from linear analytic theory; the agreement was good.

The code did, however, have some problems. In our investigation of the Bernstein waves, we found the code tended to be numerically unstable, since a high thermal velocity had to be used for the particles to see these modes; this tended to violate the CFL condition for the tail of the Maxwellian distribution. When looking at velocity space instabilities this problem became very serious. Therefore, very short time steps were required in order to carry out the computer run needed to see the physical instabilities.

Another problem encountered was that the magnetic field showed the generation of very short wavelength disturbances of the order of a few grid spacings, independent of how fine a grid was used. These were clearly unphysical and associated with the numerical method. As a means to eliminate these unphysical short wavelengths we applied a

0021-9991/92 $5.00
Copyright © 1992 by Academic Press, Inc.
All rights of reproduction in any form reserved.

Fourier filter smoothing technique to the magnetic field, which eliminated the presence of modes with wavelengths below a certain size (i.e., usually of the order of, or shorter, than the particle size of the finite sized particles). Having done so, those short wavelength waves were eliminated but energy conservation became very poor. It was observed that by reducing the time step by a factor of two the energy conservation improved by a factor of two. From this we hypothesized that the B field smoothing introduced an error in the velocity computation which was to lowest order quadratic in the time step. This enabled us to improve the calculation of the velocity by the following means. We stepped the model through two time steps of size $(\Delta t)/2$ and then went back and advanced it by one step of size Δt. Knowing the scaling of the error with Δt the difference between the two results was then used to calculate correct velocities and positions (this is identical to the deferred approach to the limit, or to the Richardson extrapolation used to solve ordinary differential equations). This method resulted in improved energy conservation by a factor of 400 for time steps which were 10 times larger. The resulting code is in most ways better for practical problems in fusion and space plasmas.

The organization of the paper is as follows. In Section 2 the model is treated analytically and a dispersion relation is derived for testing the numerical model. In Section 3 the numerical model is extensively discussed and is tested against the analytic predictions of Section 2. Finally, an application of the model to the wave studies in the JET is presented in Section 3.

1. ANALYTIC TREATMENT

We know that the time evolution of the trajectories of a collection of charged particles in their self-consistent electromagnetic fields is identical to the Vlasov equation with a singular distribution function [5] (i.e., Klimontovich equation). Furthermore, if two particle correlations are ignored in the BBGKY hierarchy obtained by ensemble averaging the Klimontovich equation, the Vlasov equation is obtained.

Before presenting our calculations, we should mention that in what follows our starting analytic equations are similar to the Vlasov-fluid equations of Freidberg [6]. However, we proceed in quite a different direction from Freidberg by using $\nabla \cdot \mathbf{j} = 0$ to eliminate $\mathbf{E}$ from the equations in order to produce an analytic scheme which closely resembles the existing numerical method for our particle simulation model; this is presented in the next section.

As a result we can use the Vlasov equation for our kinetic ions:

$$\frac{\partial f_i}{\partial t} + \mathbf{v} \cdot \frac{\partial f_i}{\partial \mathbf{r}} + \frac{e}{M_i}\left(\mathbf{E} + \frac{\mathbf{v} \times \mathbf{B}}{c}\right) \cdot \frac{\partial f_i}{\partial \mathbf{v}} = 0, \tag{1}$$

where f_i is the ion distribution function with (we assume charge neutrality)

$$n_e = n_i = \int f_i \, d\mathbf{v} = n \tag{2}$$

(n_e, n_i are electron and ion densities, respectively).

The massless electrons however satisfy the equation

$$\mathbf{E} + \frac{\mathbf{v}_e \times \mathbf{B}}{c} = 0, \tag{3}$$

where $\mathbf{v}_e$ is the electron fluid velocity. In writing Eq. (3) we assume perfect conductivity along $\mathbf{B}$, e.g., massless collisionless electrons

$$\mathbf{E} \cdot \mathbf{B} = 0. \tag{4}$$

The current $\mathbf{j}$ is therefore

$$\mathbf{j} = -en\mathbf{v}_e + e \int \mathbf{v} f_i \, d\mathbf{v}. \tag{5}$$

This current $\mathbf{j}$, according to Eq. (2) (quasineutrality assumption) must be divergence free. Thus,

$$\nabla \cdot \mathbf{j} = 0. \tag{6}$$

This is equivalent to

$$\mathbf{j}_L = 0, \tag{7}$$

where $\mathbf{j}_L$ is the longitudinal current ($\mathbf{j}_L \| \mathbf{k}$). This equation is used to find $j_{e\|}$. The relevant Maxwell equations are Faraday's law and Ampere's law without the displacement current, i.e.,

$$\nabla \times \mathbf{E} = -\frac{1}{c}\frac{\partial \mathbf{B}}{\partial t} \tag{8}$$

$$\nabla \times \mathbf{B} = \frac{4\pi}{c}\mathbf{j}. \tag{9}$$

Substituting Eq. (5) into Eq. (9) gives

$$\mathbf{j} = \frac{c}{4\pi}\nabla \times \mathbf{B} = -en\mathbf{v}_e + e \int f_i \mathbf{v} \, d\mathbf{v}, \tag{10}$$

which then implies

$$\mathbf{v}_e = \frac{e \int \mathbf{v} f_i \, d\mathbf{v} - (c/4\pi)\nabla \times \mathbf{B}}{ne}. \tag{11}$$

As a result using Eqs. (3) and (11), we have

$$\mathbf{E} = -\frac{\mathbf{v}_e \times \mathbf{B}}{c} = -\frac{\mathbf{B} \times (\nabla \times \mathbf{B})}{4\pi n e} + \frac{\mathbf{B} \times \int \mathbf{v} f_i \, d\mathbf{v}}{nc}. \tag{12}$$

Finally, using Eqs. (8) and (12), we obtain

$$\frac{\partial \mathbf{B}}{\partial t} = c\nabla \times \left\{ \frac{\mathbf{B} \times (\nabla \times \mathbf{B})}{4\pi n e} - \frac{\mathbf{B} \times \int \mathbf{v} f_i \, d\mathbf{v}}{nc} \right\}. \tag{13}$$

Likewise, using Eqs. (1) and (3), we obtain

$$\frac{\partial f_i}{\partial t} + \mathbf{v} \cdot \frac{\partial f_i}{\partial \mathbf{r}} + \frac{e}{M_i} \left\{ -\frac{\mathbf{v}_e \times \mathbf{B}}{c} + \frac{\mathbf{v} \times \mathbf{B}}{c} \right\} \cdot \frac{\partial f_i}{\partial \mathbf{v}} = 0. \tag{14}$$

Substituting $\mathbf{v}_e$ from Eq. (11) in Eq. (14) gives

$$\frac{\partial f_i}{\partial t} + \mathbf{v} \cdot \frac{\partial f_i}{\partial \mathbf{r}} + \frac{e}{M_i} \left\{ \frac{(\nabla \times \mathbf{B}) \times \mathbf{B}}{4\pi n e} - \frac{e \int f_i \mathbf{v} \times \mathbf{B} \, d\mathbf{v}}{nec} + \frac{\mathbf{v} \times \mathbf{B}}{c} \right\} \cdot \frac{\partial f_i}{\partial \mathbf{v}} = 0. \tag{15}$$

Equations (13) and (15) form the analytic basis of our model and are similar in form to the Vlasov equation with self-consistent fields. They involve only f_i and $\mathbf{B}$ ($\mathbf{E}$ does not appear explicitly).

In order to obtain an analytic dispersion relation, Eqs. (13) and (15) have to be linearized as follows. First noting that in the present model our dependent variables are the distribution function, f_i, and the magnetic field, $\mathbf{B}$, linearization is performed as follows:

$$f_i = f_{i0} + f_{i1} \tag{16}$$

$$\mathbf{B} = \mathbf{B}_0 + \mathbf{B}_1 \tag{17}$$

$$n = n_0. \tag{18}$$

In these equations quantities with subscript one are first-order perturbations and those with subscript zero are equilibrium quantities. We take f_{i0} and n_0 to be uniform throughout space. Using these relations in Eqs. (13) and (15) we obtain the following results:

$$\frac{\partial \mathbf{B}_1}{\partial t} = c\nabla \times \left\{ \frac{\mathbf{B}_0 \times (\nabla \times \mathbf{B}_1)}{4\pi n_0 e} - \frac{\mathbf{B}_0 \times \int \mathbf{v} f_{i1} \, d\mathbf{v}}{n_0 c} \right\} \tag{19}$$

$$\frac{\partial f_{i1}}{\partial t} + \mathbf{v} \cdot \frac{\partial f_{i1}}{\partial \mathbf{r}} + \frac{e}{M_i} \frac{\mathbf{v} \times \mathbf{B}_0}{c} \cdot \frac{\partial f_{i1}}{\partial \mathbf{v}} + \frac{e}{M_i} \left\{ \frac{(\nabla \times \mathbf{B}_1) \times \mathbf{B}_0}{4\pi n_0 e} - \int \frac{f_{i1} \mathbf{v} \times \mathbf{B}_0 \, d\mathbf{v}}{n_0 c} + \frac{\mathbf{v} \times \mathbf{B}_1}{c} \right\} \cdot \frac{\partial f_{i0}}{\partial \mathbf{v}} = 0. \tag{20}$$

In deriving Eq. (20) we have assumed $\nabla \times \mathbf{B}_0 = 0$.

This Eq. (20) can be cast into a much simpler form if one goes into cylindrical coordinates in velocity space. We do this now; the geometry is depicted in Fig. 1 for a case in which the magnetic field direction $\hat{b}$ is along the y axis.

Recalling that $\boldsymbol{\omega}_c = e\mathbf{B}_0/M_i c$, the third term in Eq. (20) simply is:

$$(\mathbf{v} \times \boldsymbol{\omega}_c) \cdot \nabla_v f_{i1} = -\omega_c (\mathbf{v} \times \nabla_v)_y f_{i1} = \omega_c \frac{\partial f_{i1}}{\partial \theta} \tag{21}$$

Upon assuming $f_{i1} = \tilde{f}_{i1}(\mathbf{v}, \theta) \, e^{i(\mathbf{k} \cdot \mathbf{x} - \omega t)}$ and $\mathbf{B}_1 = \delta \tilde{\mathbf{B}} e^{i(\mathbf{k} \cdot \mathbf{x} - \omega t)}$ and using Eqs. (19)–(21) and the fact that many equilibrium distributions of interest are isotropic and the last term in Eq. (20), $(\mathbf{v} \times \mathbf{B}_1/c \cdot \partial f_{i0}/\partial \mathbf{v} = 0)$[1], then the following pair of equations are obtained[2]:

$$-i\omega \, \delta \mathbf{B} = \frac{c}{4\pi n_0 e} \mathbf{k} \times ((\mathbf{k} \times \delta \mathbf{B}) \times \mathbf{B}_0) + \frac{i\mathbf{k}}{n_0} \times \left[\left(\int f_{i1} \mathbf{v} \, d\mathbf{v} \right) \times \mathbf{B}_0 \right] \tag{22}$$

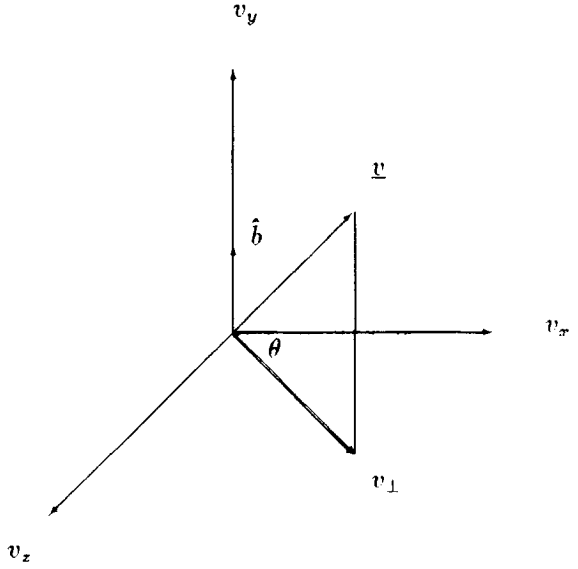

FIG. 1. The geometry in velocity space.

[1] We drop tildes, with the understanding that from now on $\delta \mathbf{B}$ and f_{i1} will be functions of ω and $\mathbf{k}$.

[2] Please note that in the term next to the last in Eq. (20) the integration in velocity space has to be carried out before making the dot product and thus the criteria which holds for the last term does not apply to it.

$$-i(\omega-\mathbf{k}\cdot\mathbf{v})f_{i1}+\omega_c\frac{\partial f_{i1}}{\partial\theta}$$
$$=-\frac{e}{M_i}\left\{\frac{1}{4\pi n_0 e}(i\mathbf{k}\times\delta\mathbf{B})\times\mathbf{B}_0 - \frac{1}{n_0 c}\left(\int f_{i1}\mathbf{v}\,d\mathbf{v}\right)\times\mathbf{B}_0\right\}\cdot\frac{\partial f_{i0}}{\partial\mathbf{v}}. \quad (23)$$

These two Equations (22) and (23), will be used to derive the analytic dispersion relation for the case of perpendicular propagation of the waves; oblique waves become heavily Landau damped and are not as important.

Using $f_{i0}(\mathbf{v})=f_{i0}(v_{||},\mathbf{v}_\perp)$, we obtain

$$\frac{\partial f_{i0}}{\partial\mathbf{v}}=\frac{\partial f_{i0}}{\partial v_{||}}\hat{b}+\frac{\partial f_{i0}}{\partial\mathbf{v}_\perp}\hat{e}_\perp, \quad (24)$$

where $\hat{e}_\perp$ is a unit vector along $\mathbf{v}_\perp$.

We perform the calculations in cylindrical coordinates in velocity space. Also, since we are only interested in studying the perpendicular propagation, we take $\mathbf{k}=(k_x,0,0)$ without any loss of generality.

In Eq. (23) the quantity inside of the brackets does not have a $\hat{y}$ component, since it is the cross product of something with $\mathbf{B}_0$, which is along $\hat{y}$. Also equilibrium distributions must be symmetric around $\mathbf{B}_0$ and, hence, independent of θ. As a result Eq. (23) becomes

$$-i(\omega-k_x v\cos\theta)f_{i1}+\omega_c\frac{\partial f_{i1}}{\partial\theta}$$
$$=\frac{e}{M_i}\left\{-\frac{1}{4\pi n_0 e}(i\mathbf{k}\times\delta\mathbf{B})\times\mathbf{B}_0+\frac{1}{n_0 c}\left(\int f_{i1}\mathbf{v}\,d\mathbf{v}\right)\times\mathbf{B}_0\right\}_x\frac{\partial f_{i0}}{\partial v}\cos\theta$$
$$+\frac{e}{M_i}\left\{-\frac{1}{4\pi n_0 e}(i\mathbf{k}\times\delta\mathbf{B})\times\mathbf{B}_0+\frac{1}{n_0 c}\left(\int f_{i1}\mathbf{v}\,d\mathbf{v}\right)\times\mathbf{B}_0\right\}_z\frac{\partial f_{i0}}{\partial v}\sin\theta. \quad (25)$$

Likewise Eq. (22) gives the following, given the fact that $\mathbf{k}\cdot\mathbf{B}_0=0$,

$$\delta\mathbf{B}=\frac{1}{\omega}\mathbf{B}_0\mathbf{k}\cdot\left(\frac{1}{n_0}\int f_{i1}(\mathbf{v})\mathbf{v}\,d\mathbf{v}\right). \quad (26)$$

As a result, $\delta\mathbf{B}\parallel\mathbf{B}_0$ as expected for perpendicular propagating waves.

Next we solve for $(1/n_0)\int f_{i1}(\mathbf{v})\mathbf{v}\,d\mathbf{v})\times\mathbf{B}_0$ from Eq. (22) in terms of known quantities such as $\delta\mathbf{B}$, $\mathbf{B}_0$ and substitute it into Eq. (25).

From Eq. (22) one simply obtains

$$\delta\mathbf{B}=-\frac{1}{\omega}\mathbf{k}\times\left[\left(\frac{1}{n_0}\int f_{i1}(\mathbf{v})\mathbf{v}\,d\mathbf{v}\right)\times\mathbf{B}_0\right]. \quad (27)$$

Taking the cross product of this equation with $\mathbf{k}$ gives

$$\mathbf{k}\times\delta\mathbf{B}=-\frac{1}{\omega}(\mathbf{kk}-k^2\underline{\underline{|\!|}})\cdot\left[\left(\int\frac{1}{n_0}f_{i1}(\mathbf{v})\mathbf{v}\,d\mathbf{v}\right)\times\mathbf{B}_0\right]. \quad (28)$$

If one knows $(\mathbf{kk}-k^2\underline{\underline{|\!|}})^{-1}$ ($\underline{\underline{|\!|}}$ is the unit dyadic tensor), then one can compute $(\int(1/n_0)f_{i1}(\mathbf{v})\mathbf{v}\,d\mathbf{v})\times\mathbf{B}_0$. In this case since $\mathbf{k}=(k_x,0,0)$,

$$\mathbf{kk}-k^2\underline{\underline{|\!|}}=\begin{pmatrix}0&0&0\\0&-k_x^2&0\\0&0&-k_x^2\end{pmatrix} \quad (29)$$

and so the determinant of $(\mathbf{kk}-k^2\underline{\underline{|\!|}})$ is zero and therefore it does not have an inverse. In order to make it invertible, let us add an infinitesimal number ε times the identity matrix to it, and then compute $(\int(1/n_0)f_{i1}(\mathbf{v})\mathbf{v}\,d\mathbf{v})\times\mathbf{B}_0$ in the limit as $\varepsilon\to 0$; Eq. (28) is identical to

$$\lim_{\varepsilon\to 0}\frac{-1}{\omega}(\varepsilon\underline{\underline{|\!|}}+\mathbf{kk}-k^2\underline{\underline{|\!|}})\cdot\left[\left(\int\frac{1}{n_0}f_{i1}(\mathbf{v})\mathbf{v}\,d\mathbf{v}\right)\times\mathbf{B}_0\right]=\mathbf{k}\times\delta\mathbf{B}. \quad (30)$$

This equation after some algebra reduces to

$$\left(\int\frac{1}{n_0}f_{i1}(\mathbf{v})\mathbf{v}\,d\mathbf{v}\right)\times\mathbf{B}_0=\lim_{\varepsilon\to 0}(-\omega)\begin{pmatrix}0\\0\\\dfrac{k_x}{-k_x^2+\varepsilon}\delta B_y\end{pmatrix}=\begin{pmatrix}0\\0\\\dfrac{\omega}{k_x}\delta B_y\end{pmatrix}. \quad (31)$$

This implies that

$$\left(\int\frac{1}{n_0}f_{i1}(\mathbf{v})\mathbf{v}\,d\mathbf{v}\right)\times\mathbf{B}_0=\left[\left(\int\frac{1}{n_0}f_{i1}(\mathbf{v})\mathbf{v}\,d\mathbf{v}\right)\times\mathbf{B}_0\right]_z\hat{z}=\frac{\omega}{k_x}\delta B_y\hat{z}. \quad (32)$$

Also, using vector identities it is true that

$$-i(\mathbf{k}\times\delta\mathbf{B})\times\mathbf{B}_0 = ik_x(\mathbf{B}_0\cdot\delta\mathbf{B})\hat{x}. \tag{33}$$

Thus using Eqs. (32) and (33) in Eq. (25) gives

$$-i(\omega - k_x v\cos\theta)\, f_{i1} + \omega_c \frac{\partial f_{i1}}{\partial\theta} = \frac{e}{M_i}\left(\frac{1}{4\pi n_0 e} ik_x\, \delta B_y B_0\right)\frac{\partial f_{i0}}{\partial v}\cos\theta + \frac{e}{M_i c}\frac{\omega}{k_x}\delta B_y \frac{\partial f_{i0}}{\partial v}\sin\theta. \tag{34}$$

This equation is simply a first-order differential equation for f_{i1}; i.e., it has the form

$$p(\theta)\, f_{i1} + \frac{\partial f_{i1}}{\partial\theta} = g(\theta), \tag{35}$$

where $p(\theta)$, $g(\theta)$, and v and κ are defined to be

$$p(\theta) = -i\left(\frac{\omega}{\omega_c} - \frac{\mathbf{k}\cdot\mathbf{v}}{\omega_c}\right) = -i(v - r\cos\theta) \tag{36}$$

$$g(\theta) = \left(\frac{1}{4\pi n_0 M_i\omega_c} ik_x B_0\cos\theta + \frac{e\omega}{M_i c k_x \omega_c}\sin\theta\right) \times \delta B_y \frac{\partial f_0}{\partial v} \tag{37}$$

$$v = \frac{\omega}{\omega_c}\ \kappa = \frac{k_x v}{\omega_c}. \tag{38}$$

As a result the solution to the Eq. (34) is obtained upon multiplying it by an integrating factor $\mu(\theta)$ defined to be

$$\mu(\theta) = e^{\int p\, d\theta} = e^{-i(v\theta - \kappa\sin\theta)}. \tag{39}$$

With this, the solution to Eq. (34) is

$$f_{i1}(\theta) = \frac{1}{\mu(\theta)}\int_{-\infty}^{\theta} \mu(\theta')\, g(\theta')\, d\theta' = e^{i(v\theta - \kappa\sin\theta)}\int_{-\infty}^{\theta} \mu(\theta')\, g(\theta')\, d\theta' = e^{i(v\theta - \kappa\sin\theta)}\int_{-\infty}^{\theta} e^{-i(v\theta' - \kappa\sin\theta')} \times\left(\frac{ik_x B_0\cos\theta'}{4\pi n_0 M_i\omega_c} + \frac{e\omega\sin\theta'}{M_i c k_x\omega_c}\right)\delta B_y \frac{\partial f_0}{\partial v}(\theta')\, d\theta'. \tag{40}$$

Substituting this $f_{i1}(\theta)$ into Eq. (26) and using the fact that $\mathbf{B}_0 = (0, B_0, 0)$, $\mathbf{k} = (k_x, 0, 0)$ with $\mathbf{k}\cdot\mathbf{v} = k_x v\cos\theta$ finally results in the following dispersion relation when δB_y is eliminated from both sides of the resulting equation:

$$1 = \int_{-\infty}^{\infty} dv_{\parallel}\int_0^{\infty} v^2\, dv \int_0^{2\pi} d\theta \int_{-\infty}^{\theta} d\theta'\, e^{iv(\theta-\theta') - i\kappa(\sin\theta - \sin\theta')}\frac{\partial f_{i0}}{\partial v} \times\cos\theta\left[\frac{ik_x^2 c_A^2}{\omega\omega_c}\cos\theta' + \sin\theta'\right]. \tag{41}$$

Since $f_{i0} = f_{i0}(v_{\parallel}, v_{\perp})$, it does not have any explicit θ dependence; the integrations over θ and θ' can be carried out in much the same way as was done by Bernstein [11] (please see the Appendix A). The following analytic dispersion relation is obtained for a Maxwellian background distribution function:

$$1 + \int_0^{+\infty} v^2\, dv\left[-2\frac{ve^{-v^2/a_\perp^2}}{\pi a_\perp^4}\right]\times\left\{\left(\frac{k_\perp c_A^2\pi}{\omega v}\right) \times\left(\sum_{n=-\infty}^{+\infty}\left[\frac{[(2n+1)\omega - 2n(n+1)\omega_c]\,\omega_c}{(\omega - n\omega_c)(\omega - (n+1)\omega_c)} \times J_n\left(\frac{k_\perp v}{\omega_c}\right)J_{n+1}\left(\frac{k_\perp v}{\omega_c}\right)\right]\right) + \sum_{n=-\infty}^{+\infty}\frac{\pi}{2} \times\left[\frac{[J_n(k_\perp v/\omega_c)]^2}{\omega + (1-n)\omega_c} - \frac{[J_n(k_\perp v/\omega_c)]^2}{\omega - (1+n)\omega_c}\right]\right\} = 0, \tag{42}$$

where $v = v_\perp$, ω_c is the ion cyclotron frequency, and c_A is the Alfven velocity, $a_\perp$ is the perpendicular thermal velocity of the ions.

2. NUMERICAL MODEL AND ITS TEST

In this section we shall present the numerical algorithm of our hybrid model with its tests against analytic predictions. Some words about related efforts in hybrid modeling of plasmas is in order. Two of the best examples of authors who have developed hybrid models and successfully applied them to plasma physics problems are those of Winske [7] and Horowitz [8]. Regarding numerical techniques and methodology, the main difference between their methods and our work is the successful elimination of **E** in our scheme and the consequent elimination of extra computation imposed by the **E** field push equations.

The relevant equations for our particle model are

$$\frac{d\mathbf{r}_i}{dt} = \mathbf{v}_i \tag{43}$$

$$\frac{d\mathbf{v}_i}{dt} = \frac{e}{M_i}\left(\mathbf{E} + \frac{\mathbf{v}_i\times\mathbf{B}}{c}\right); \tag{44}$$

i is the subscript specifying each and every ion. Equations (43) and (44) are identical to the Vlasov Equation (14) as mentioned before. Using $\mathbf{v}'$ as the average ion velocity (i.e., $\mathbf{v}' = \int \mathbf{v} f_i \, d\mathbf{v}/n$) in a given cell in Eq. (12) gives

$$\mathbf{E} = -\frac{\mathbf{B}\times(\nabla\times\mathbf{B})}{4\pi ne} + \frac{\mathbf{B}\times\mathbf{v}'}{c}. \tag{45}$$

Clearly $\mathbf{v}'$ in Eq. (45) is the same as the ion fluid velocity, $\mathbf{v}_f$, associated with a grid cell. Using Eqs. (44) and (45) gives

$$\frac{d\mathbf{v}_i}{dt} - \frac{e}{M_i}\frac{(\mathbf{v}_i - \mathbf{v}')\times\mathbf{B}}{c} = -\frac{e}{M_i}\frac{\mathbf{B}\times(\nabla\times\mathbf{B})}{4\pi ne}. \tag{46}$$

Upon using Eq. (45) in Eq. (8) we obtain

$$\frac{\partial\mathbf{B}}{\partial t} = c\nabla\times\left\{\frac{\mathbf{B}\times(\nabla\times\mathbf{B})}{4\pi ne} - \frac{\mathbf{B}\times\mathbf{v}'}{c}\right\}. \tag{47}$$

At this point we normalize Eqs. (46) and (47), using the scheme,

$$\tilde{\mathbf{B}} = \frac{\mathbf{B}}{\sqrt{4\pi\rho_0}\, c_s}, \qquad \nabla = \frac{1}{\Delta}\tilde{\nabla} \tag{48}$$

$$\frac{\partial}{\partial t} = \frac{c_s}{\Delta}\frac{\partial}{\partial \tilde{t}}, \qquad \tilde{\mathbf{v}} = \frac{\mathbf{v}}{c_s}. \tag{49}$$

Then Eqs. (46) and (47) reduce to the following set (tildes are dropped):

$$\frac{d\mathbf{v}_i}{dt} = \frac{\Delta}{\lambda}(\mathbf{v}_i - \mathbf{v}')\times\mathbf{B} + \frac{n_0}{n}(\nabla\times\mathbf{B})\times\mathbf{B} \tag{50}$$

$$\frac{\partial\mathbf{B}}{\partial t} = \nabla\times\left\{\frac{\lambda}{\Delta}\frac{n_0}{n}\mathbf{B}\times(\nabla\times\mathbf{B}) + \mathbf{v}'\times\mathbf{B}\right\}; \tag{51}$$

please note that $\lambda = c/\omega_{pi}$ is the collisionless skin depth for the ions, and $\Delta = c/\omega_{pi}$ also is just the grid spacing; both have unit values in computer units; $c_s = \sqrt{T_e + T_i/M}$.

Equations (50) and (51) have been pushed in the model in the following way: $\mathbf{B}$, the particle positions $\mathbf{r}_i$ (and the density n) are known at integer time steps, the particle velocities are known at half-integer time steps as illustrated in part (a) of Fig. 2. First $\mathbf{v}_i$ is pushed from time step $l-\frac{1}{2}$ to time step l using Eq. (50) and the values of $\mathbf{B}$ at l, $\mathbf{v}_i$, and $\mathbf{v}'$ at $l-\frac{1}{2}$. Note that $\mathbf{v}' = \mathbf{v}_f$, where $\mathbf{v}_f$ is the ion fluid (average per cell) velocity which is obtained using the area weighting interpolation scheme extensively discussed in [3, 4]. Next, $\mathbf{B}$ is pushed from time step l to $l+\frac{1}{2}$, using Eq. (51) and the value of $\mathbf{v}'$ and the spatial average of $\mathbf{B}$ at time step l. This is the auxiliary step of the Lax-Wendroff scheme.

Next, the ion velocities $\mathbf{v}_i$ are pushed again from the time step l to $l+\frac{1}{2}$, using the values of $\mathbf{B}$, $\mathbf{v}_i$, and $\mathbf{v}'$ at l. These values of $\mathbf{B}$ and $\mathbf{v}'$ at $l+\frac{1}{2}$ are then used to advance $\mathbf{B}$ all the way to $l+1$. This is the main step of the Lax–Wendroff scheme; both steps together form a Lax–Wendroff method for computing $\mathbf{B}$. The particles are used to compute the plasma density n and the average ion velocity per cell, $\mathbf{v}'$, twice at each time step, once for the half time step and another time for the full time step, using the standard area weighting method. A summary of all of these steps is given in Table I, where $\bar{\bar{1}}$ is the unit dyadic tensor, and the subscripts i, j refer to grid locations, while a is the cutoff length in doing the $\mathbf{B}$ field smoothing, i.e., the length which corresponds to the shortest allowable wavelength in the simulation. Pressure simply does not appear here, since we are treating the ions kinetically and, thus, they respond to the Lorentz force and not to the fluid pressure.

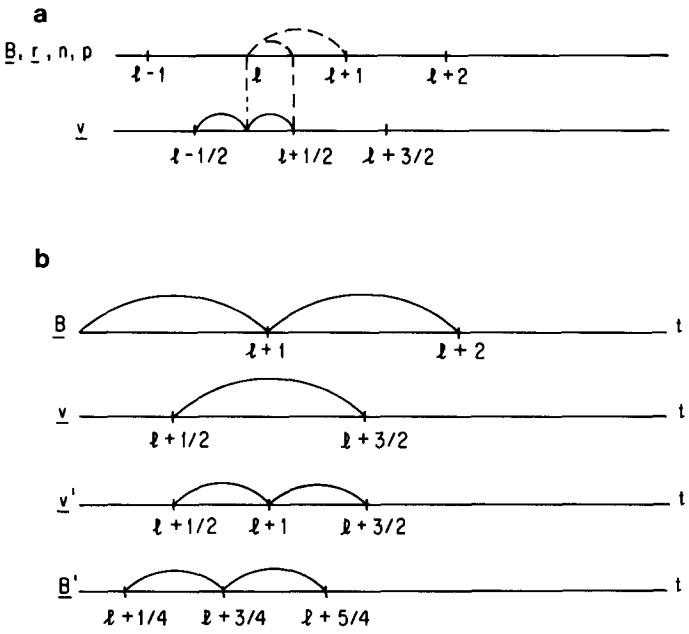

FIG. 2. Time stepping scheme for $\mathbf{B}$, $\mathbf{r}$, n, $\mathbf{v}$ in the parallel run.

Simulations were performed using the geometry of Fig. 3 and no smoothing of $\mathbf{B}$ ($a=0$). Plotting contours of magnetic field strength showed that very short wavelength disturbances on the order of grid spacing were produced as shown in Fig. 4. As Fig. 5 also indicates, using a finer grid system only resulted in shorter wavelength disturbances, even though the ratio of the grid size to the Larmor radius was much smaller. Wavelengths of the order of the grid spacings are unphysical and must be generated by the numerical method of solving for $\mathbf{B}$.

Unphysical short wavelengths can cause artificial numerical heating of the ions [9]. This also makes sense physically, since unphysical short wavelengths are like a heat bath in which the particles are embedded. Because of this we

TABLE I

Numerical Algorithm of the Vlasov Ion Fluid Electron Model

1. Compute density n^l from particle positions by interpolation
2. Compute the magnetic force:

$$\mathbf{F}_B^l = \frac{n_0}{n^l}\left[-\nabla\cdot\left(\frac{B^2}{2}\bar{\bar{\mathrm{II}}} - \mathbf{BB}\right)\right]^l$$

3. Push the ion velocities half a time step:

$$\mathbf{v}^l = \mathbf{v}^{l-1/2} + (\mathbf{v}^{l-1/2} - \mathbf{v}'^{l-1/2})\times\mathbf{B}^l\,\Delta t/2 + \mathbf{F}_B^l\,\Delta t/2$$

4. Compute average ion velocities per cell $\mathbf{v}'^l$ from particle velocities
5. Push **B** half a time step as the auxiliary step of the Lax–Wendroff scheme:

$$\mathbf{B}^{l+1/2} = \langle\mathbf{B}\rangle^l + \left(\nabla\times\left[\mathbf{v}'^l\times\mathbf{B}^l + \frac{\lambda}{\Delta}\frac{n_0}{n^l}\nabla\cdot\left(\frac{B^2}{2}\bar{\bar{\mathrm{II}}} - \mathbf{BB}\right)^l\right]\right)\Delta t/2$$

where $\langle\mathbf{B}\rangle_{ij}^l = \frac{1}{4}(B_{i+1,j}^l + B_{i-1,j}^l + B_{i,j+1}^l + B_{i,j-1}^l)$ in two dimensions

6. Smoothing of **B**, $\mathbf{v}'$, n, e.g.,

$$\mathbf{B}_{i,j} \xrightarrow{\text{FFT}} \tilde{\mathbf{B}}(\mathbf{k}) \longrightarrow \tilde{\mathbf{B}}'(\mathbf{k}) = e^{-k^2n^2/2}\tilde{\mathbf{B}}(\mathbf{k}) \xrightarrow{\text{FFT}} \mathbf{B}_{i,j}$$

7. Push the ion velocities another half a time step:

$$\mathbf{v}^{l+1/2} = \mathbf{v}^l + (\mathbf{v}^l - \mathbf{v}'^l)\times\mathbf{B}^l\,\Delta t/2 + \mathbf{F}_B^l\,\Delta t/2$$

8. Push positions half a time step:

$$\mathbf{r}^{l+1/2} = \mathbf{r}^l + \mathbf{v}^{l+1/2}\,\Delta t/2$$

9. Compute average ion velocities per cell $\mathbf{v}'^{l+1/2}$ by interpolation.
10. Push **B** a full time step as the main step of the Lax–Wendroff scheme:

$$\mathbf{B}^{l+1} = \mathbf{B}^l + \left(\nabla\times\left[\mathbf{v}'^{l+1/2}\times\mathbf{B}^{l+1/2} + \frac{\lambda}{\Delta}\frac{n_0}{n^{l+1/2}}\nabla\cdot\left(\frac{B^2}{2}\bar{\bar{\mathrm{II}}} - \mathbf{BB}\right)^{l+1/2}\right]\right)\Delta t$$

11. Smoothing of **B**, $\mathbf{v}'$, n, e.g.,

$$\mathbf{B}_{i,j} \xrightarrow{\text{FFT}} \tilde{\mathbf{B}}(\mathbf{k}) \longrightarrow \tilde{\mathbf{B}}'(\mathbf{k}) = e^{-k^2n^2/2}\tilde{\mathbf{B}}(\mathbf{k}) \xrightarrow{\text{FFT}} \mathbf{B}_{i,j}$$

12. Push positions half a time step: $\mathbf{r}^{l+1} = \mathbf{r}^{l+1/2} + \mathbf{v}^{l+1/2}\,\Delta t/2$

Note. Initially we have: $\mathbf{B}^l$, $\mathbf{v}^{l-1/2}$, $\mathbf{r}^l$

eliminated such short wavelength waves by applying a **k** space filter (**a** is the cutoff length):

$$\mathbf{B}'(\mathbf{k}) = \mathbf{B}(\mathbf{k})\,e^{-k^2a^2/2}. \tag{52}$$

The quantity a determines the maximum k (minimum wavelength) and is adjustable to determine its effects on results.

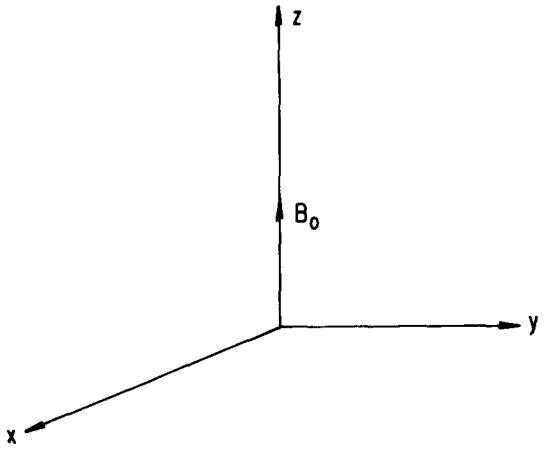

FIG. 3. Geometry of the plasma model.

As Fig. 6 indicates, the short wavelength disturbances were eliminated as a result. This resulted in the energy conservation becoming very poor. We observed, roughly, an energy gain of 10% in a few cyclotron periods. The energy conservation improved by a factor of two when the time step was halved, e.g., $\Delta w = 14\%$ in $\omega_{ci}t = 48$ for $\Delta t = 0.00625/\omega_{ci}$, while $\Delta w = 7\%$ in $\omega_{ci}t = 48$ for $\Delta t = 0.003125/\omega_{ci}$ (w is the total energy of the system and Δw is its change). Consequently for $\Delta t \to \Delta t/2$, $\Delta w \to \Delta w/2$ at the same value of $\omega_{ci}t$; this indicates a linear dependence

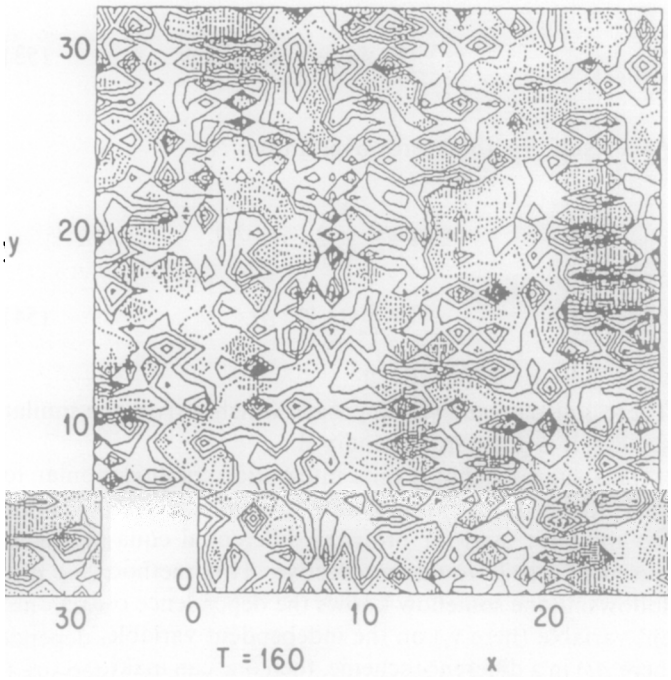

FIG. 4. **B** field contour plot of a 32×32 system without smoothing. Thermal runs. $V_T = 0.1$. $B_{oz} = 4.0$.

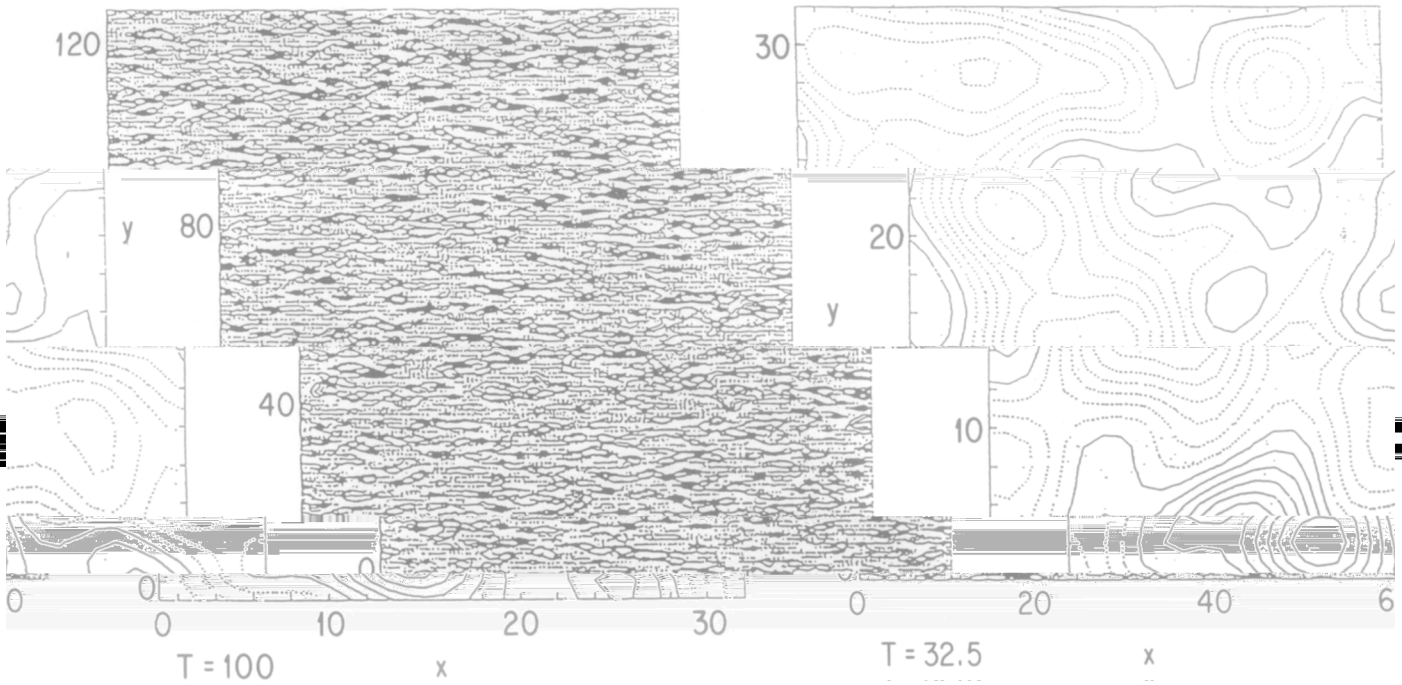

FIG. 5. **B** field contour plot of a 64×128 system without smoothing.

FIG. 6. **B** field contour plot of a 32×32 system with smoothing. Thermal run. $V_T = 1.0$. $B_{oz} = 0.25$.

of Δw_{tot} on Δt. Assuming that the error is in the computation of $\mathbf{v}$ (where most of the energy is), we concluded that the error in v_i (δv_i) is $\delta v_i \propto \varepsilon_i (\Delta t)^2$ for each time step and is cumulative. The error introduced in a given time step is

$$\Delta w = \sum_i [(v_i + \delta v_i)^2 - v_i^2]$$

$$\cong \sum_i 2 v_i \, \delta v_i = \sum_i 2 v_i \varepsilon_i (\Delta t)^2. \tag{53}$$

As a result, the total error over a time T is

$$\Delta w_{\text{tot}} \cong 2 \frac{T}{\Delta t} \sum_i v_i \varepsilon_i (\Delta t)^2$$

$$= \sum_i 2 v_i T \varepsilon_i \, \Delta t. \tag{54}$$

There is also an analytic approach which arrives at a similar scaling; it is given in Appendix B.

This suggests that a time integration method similar to the so-called Richardson extrapolation or the deferred approach to the limit used for ordinary differential equations discussed in [10] would be effective. This method works as follows: if one somehow knows the dependence of a dependent variable (here $\mathbf{v}_i$) on the independent variable step size (here Δt) in a difference scheme, then one can make two or more computations of that dependent variable using different step sizes and use those results to compute the zero order dependence or the "correct value" of the dependent variable.

In order to eliminate the error we made parallel runs with Δt and $\Delta t/2$, and at the end of each full time step we corrected the velocity in the following manner: If $\mathbf{v}_i'$ indicates the velocity from the $\Delta t/2$ run, then upon going from time step $l + \frac{1}{2}$ to $l + \frac{3}{2}$, we introduce an error of $\varepsilon_i (\Delta t/2)^2$ for each time step and $\mathbf{v}_i'$ is given by

$$\mathbf{v}_i'\left(l + \frac{3}{2}\right) = \mathbf{v}_{ic}\left(l + \frac{3}{2}\right) + 2\varepsilon_i \left(\frac{\Delta t}{2}\right)^2, \tag{55}$$

where $\mathbf{v}_{ic}$ is the correct velocity at $l + \frac{3}{2}$. If we push $\mathbf{v}_i(l + \frac{1}{2})$ one time step Δt, we introduce one error of size $\varepsilon_i \, \Delta t^2$ and $\mathbf{v}_i$ is

$$\mathbf{v}_i(l + \tfrac{3}{2}) = \mathbf{v}_{ic}(l + \tfrac{3}{2}) + \varepsilon_i (\Delta t)^2. \tag{56}$$

Upon eliminating ε_i from Eq. (55) and Eq. (56) one obtains for the correct velocity:

$$\mathbf{v}_{ic}(l + \tfrac{3}{2}) = 2\mathbf{v}_i'(l + \tfrac{3}{2}) - \mathbf{v}_i(l + \tfrac{3}{2}). \tag{57}$$

Figures 2(b) and 7 illustrate this method and its flow chart, respectively.

As a result, conservation of energy was improved by a factor of 400 for the same time step and time duration as shown in Figs. 8 and 9. The improvement was adequate to increase the time step by a factor of 10.

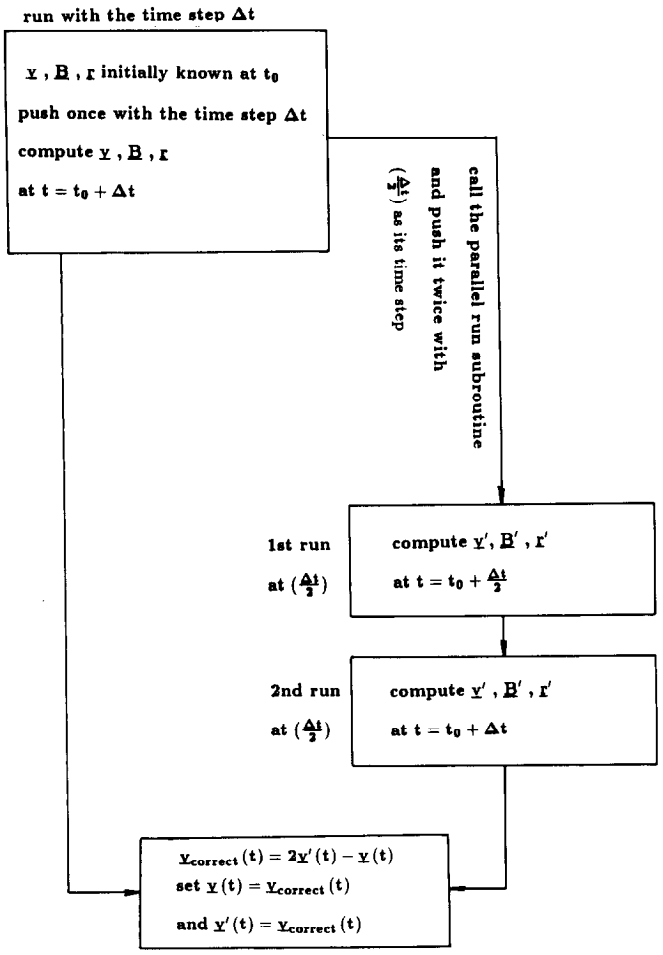

FIG. 7. Flow chart of the parallel scheme.

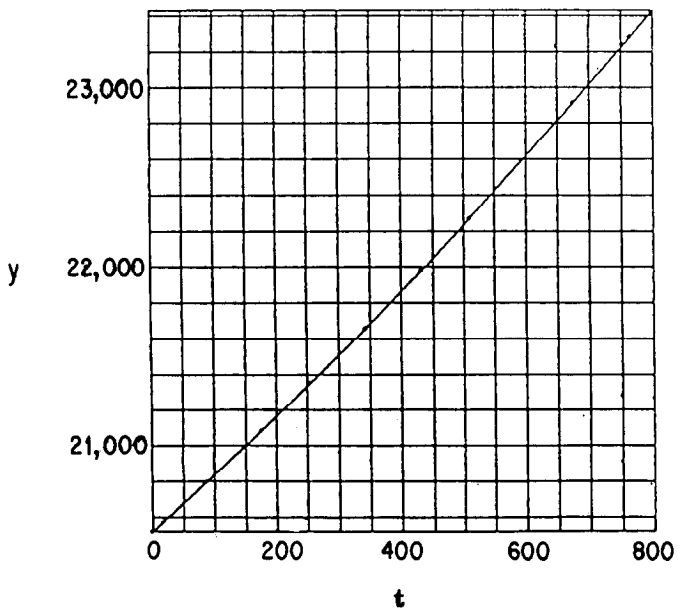

FIG. 8. Total energy (y) versus time (t) before the insertion of the "parallel run" subroutine with the time step $\Delta t = 0.00625/\omega_{ci}$. The error in energy = 14.1 %.

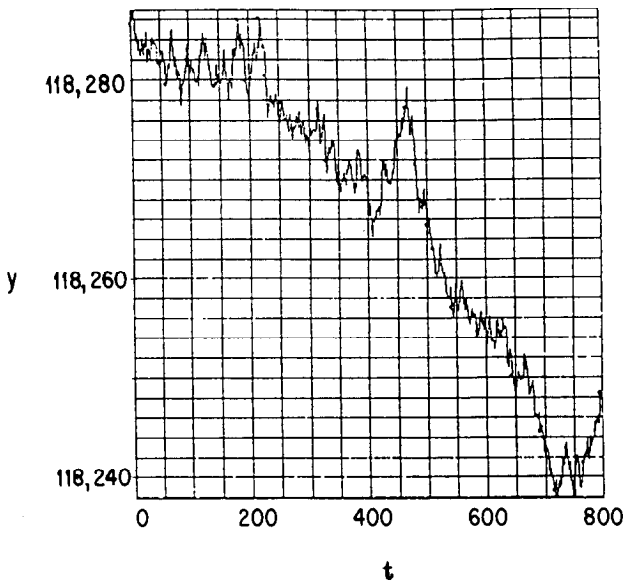

FIG. 9. Total energy (y) versus time (t) after the insertion of the "parallel run" subroutine with the time step $\Delta t = 0.00625/\omega_{ci}$. The error in energy = 0.032 %.

A reasonable question to raise at this point is: we made the corrections on only the velocity, but what about the magnetic field and the particle positions? Correcting the velocity after each Δt really gives most of the corrections to $\mathbf{r}_i$ because $\mathbf{r}_i$ is pushed by $\mathbf{v}_i$ and if we keep the correct $\mathbf{v}_i$, errors in $\mathbf{r}_i$ will stay very small. Since the same is true for pushing **B**, we can expect the same conclusion to be true about it as for $\mathbf{r}_i$. As Figs. 10 and 11 indicate the fields taken with the half-time step pusher and that with the full time

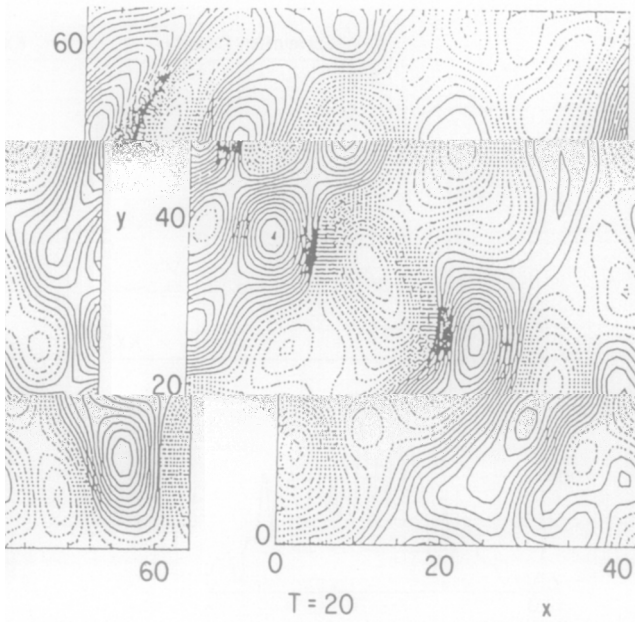

FIG. 10. Contour plot of **B** field at half time step.

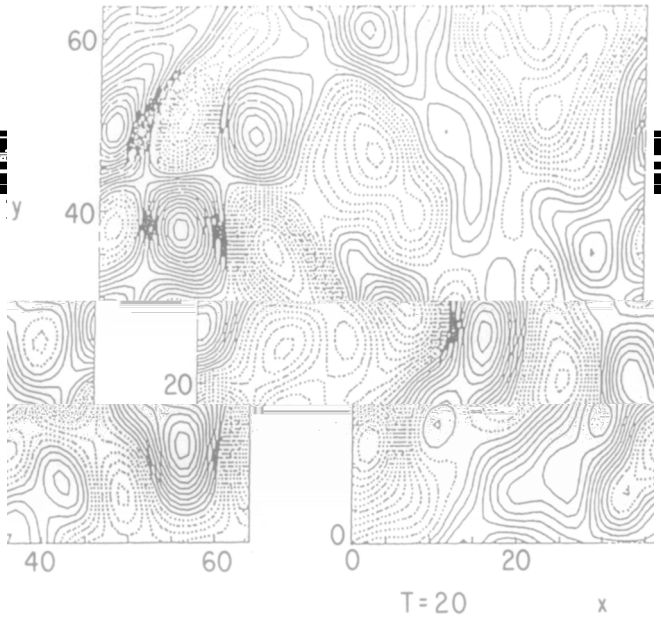

FIG. 11. Contour plot of **B** field at full time step.

step pusher at roughly the same time[3] (note, they are off in time by $\Delta t/4$ as Fig. 2(b) shows) are then quite close. As a result we did not introduce these corrections, although introducing them might well result in some further improvement.

[3] That is, about 100 time steps.

Finally the model was tested against linear analytic prediction of the dispersion relation (Eq. (42)). Figure 12 shows a typical power spectrum. One clearly sees the existence of clear peaks at integer multiples of the ion

simulation results (asterisks are taken from the power spectrum of the density). The agreement is good in light of the finite sized grids and finite sized nature of the particles; corrections for these effects should improve the agreement. There is, however, in general a branch in which $\omega \to 0$ as $k_\perp \to 0$ and it is missing in that figure. We believe this is because this figure corresponds to a case in which the Alfven speed is less than the ion thermal speed, $c_A = 0.125 \ll c_T = 1.00$ with c_T the thermal speed of the ions; i.e., for such a case these modes should show something like Landau damping. The interested reader is referred to Fig. 21 for the dispersion relation of a simulation in which $c_A \cong 6.8$ and $c_T \cong 0.82$; one can clearly see a branch in which $\omega \to 0$ as $k_\perp \to 0$. A more detailed discussion of those results is given in the application section.[4] Finally Fig. 14 shows the orbits of sample particles taken at random. The circular orbits clearly show the ion motion at ω_{ci} which should give rise to Bernstein like waves.

In conclusion the model has been given a rigourous set of tests and passed them all. It has so far been used to study instabilities due to an ion ring in velocity space along with

[4] Fredricks [15] has also derived a fully electromagnetic dispersion relation yielding a similar mode.

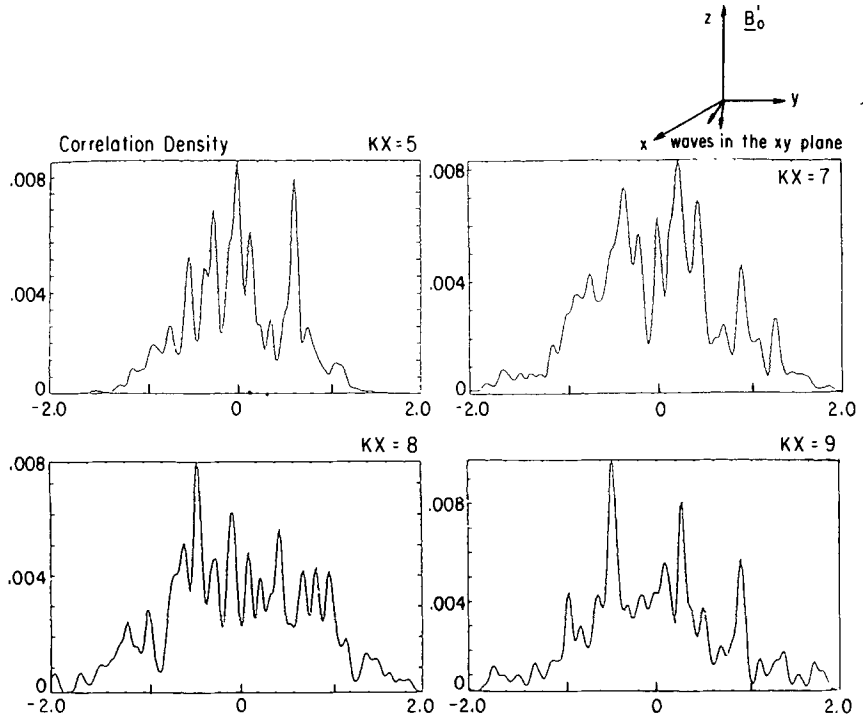

FIG. 12. A typical power spectrum for the density, $\omega_c = 0.125$ (simulation results).

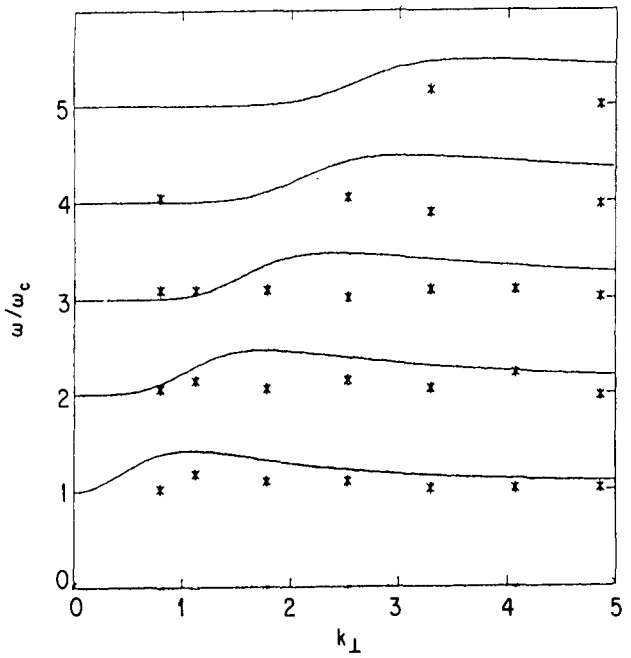

FIG. 13. Analytic versus simulation dispersion relations for perpendicular propagation.

such important effects as those that give nonlinear wave saturation. As a direct application, the model has successfully explained the generation of fluctuations which have been observed on the JET and TFTR tokamaks around harmonics as well as half-harmonics of the ion cyclotron frequency which we show in the applications section. Also it has been used to study the interaction of an outflowing cometary gas and the solar wind with successes in qualitatively demonstrating complex plasma effects shown in the AMPTE experimental results [14]. We have also developed a three-dimensional version of this code which we believe could be applied to a wide range of problems in fusion and space plasma physics. For more general conclusions please refer to the final section.

3. APPLICATION: SIMULATION OF THE ION CYCLOTRON EMISSION IN THE JET TOKAMAK

One of the dominant means of heating tokamak plasmas has been through the injection of fast neutral beams. The ionization of these neutral beams predominantly happens

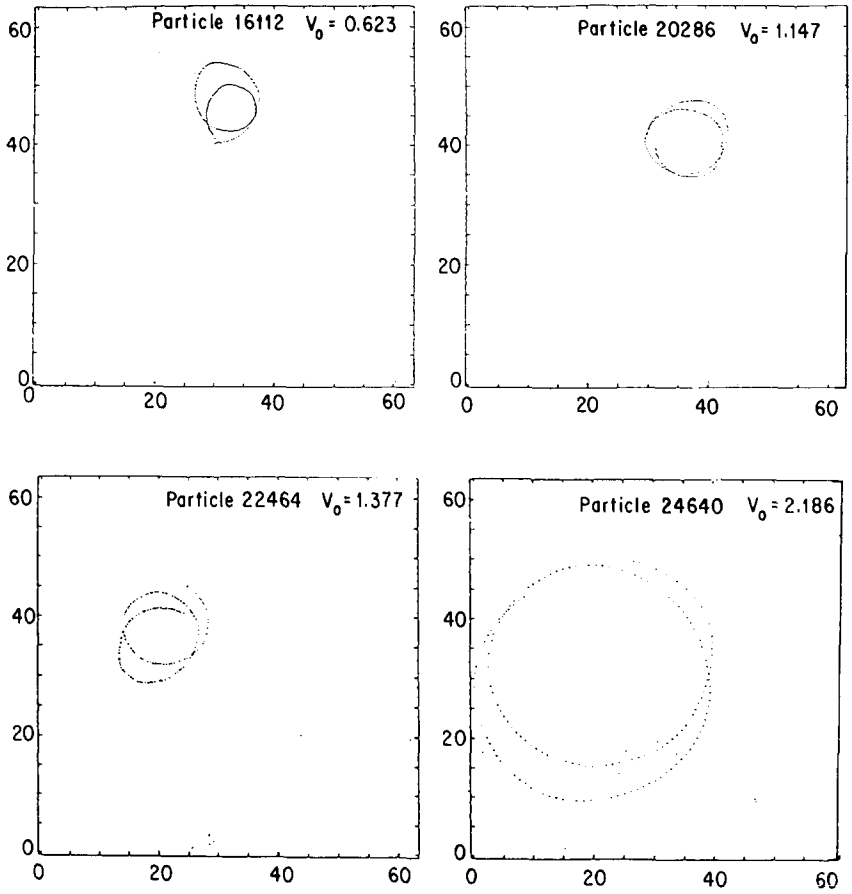

FIG. 14. Trajectory of some particles plotted at random taken at $T = 6(2\pi/\omega_c)$.

through charge exchange with the hydrogen ions of the plasma; the resultant high energy ions are trapped in the magnetic fields of the tokamak.

Recently in the JET and TFTR tokamaks they have observed superthermal ion-cyclotron emission from ohmic- and neutral-beam-heated discharges [12]. For neutral hydrogen beam injection in a deuterium plasma, in particular, they have observed very sharp peaks at multiple harmonics and half-harmonics of the cyclotron frequency of the hydrogen ions. If the neutral beams are not turned on, no sharp peaks at these frequencies are observed. Please refer to Fig. 15.

The authors (Cottrell *et al.*) of the paper [12] conjectured that these peaks can be attributed to instabilities arising from the "anisotropic velocity distribution created either by hydrogen neutral-beam injection (NBI) or by large radial orbit excursions of the centrally born fusion products." The source of energy for such instabilities would be ring or shell distributions in ion velocity space created by injection of the ions or by fusion reactions. Here, we report on simulations testing both of these conjectures; i.e., simulating both neutral beam injection and the fusion product experiments. We used our Vlasov ion fluid electron model to model the JET experiments; i.e., the analytic treatment which led to the dispersion relation Eq. (42), and Figs. 12, 13, and 14 form much of the basis for the material of this section.

3.1. *Simulation of the Neutral Beam Injection*

In the experiments the electron density was $n_e = 10^{14}/\text{cm}^3$, the electron temperature was $T_e = 7.5$ KeV, the ion temperature $T_i = 15.0$ KeV, the beam drift energy was 45.0 KeV, the electron cyclotron frequency $\omega_{ce} = 100$ GHz, so our approximation of massless electrons is good. The ion cyclotron frequency $\omega_{ci} = 50$ MHz, the Alfven velocity $c_A = 10^7$ m/s, the injection of the neutral beams were performed at 58° with respect to the toroidal magnetic field of the tokamak; the magnetic field was not homogeneous (it had a hyperbolic dependence on the radial distance from the center of the torus) and the ionization time of a neutral was on the average 10^{-7} s, during which time the neutrals penetrated 30 cm or so into the plasma. We adjusted all the simulation parameters to these; the normalizations outlined earlier (Eqs. (48) and (49) were used and the ratio of the Alfven speed to the ion acoustic speed was adjusted to the above parameters; i.e., simulation velocities were computed upon normalizing with respect to the $c_s = \sqrt{(T_i + T_e/M}$

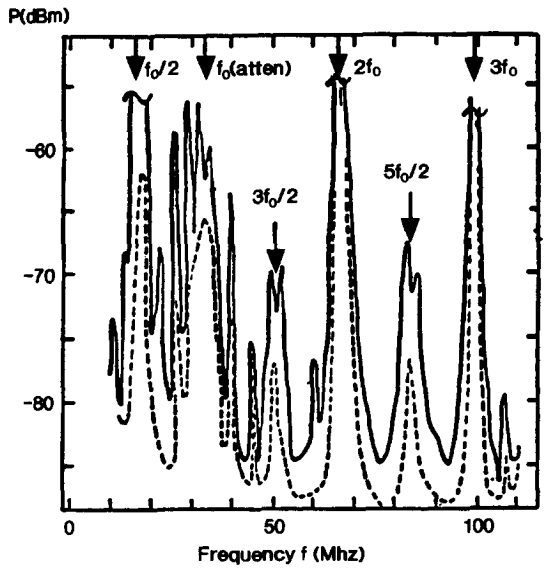

FIG. 15. Ion cyclotron emission spectrum measured before and during 4-MW H^0 neutral-beam injection into a D^+ limiter plasma [12, 13]. ICRF discharge: $f_0 = 33.4$ MHz; ---, $P_{RF} = 30$ kW; ———; $P_{RF} = 100$ kW; ~ = peak saturation.

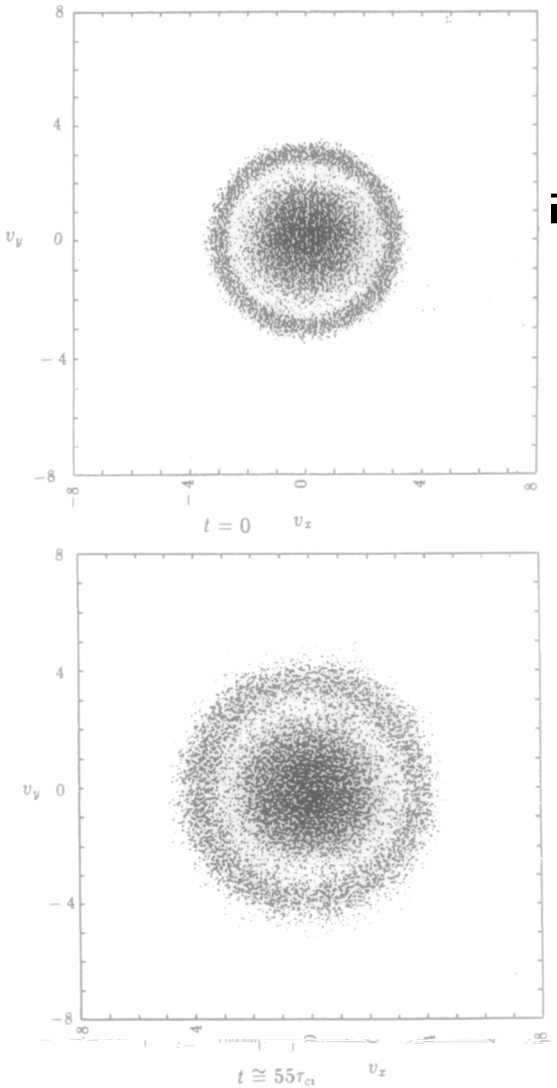

FIG. 16. Evolution of a ring in velocity space with a drift speed perpendicular to the external magnetic field $\mathbf{B}_0 = B_0\hat{z}$.

with the T_i and T_e as given by the above. With these then, $\omega_{ci} = 6.87$ in the simulations, where ω_{ci} corresponds to the protons' or H^+'s gyrofrequency.

In order to simulate such an experiment and study its wave modes, we took advantage of the fact that in the experiments one has one species of the ions at a relative drift speed with respect to another. As a first step, we did an initial value simulation of a group of energetic ions interacting with a background plasma; i.e., we simulated a ring in velocity space (ring velocity perpendicular to $\mathbf{B}_0$) interacting with a background depicted in Fig. 16. The ring comprised $\frac{1}{3}$ of the total plasma. The temperature of the energetic ring was 0.8155 in computer units corresponds to 15 KeV as in the real experiment, while its speed of 3.00 in computer units corresponds to 200 KeV. As mentioned, the beam drift energy in the real experiment was only 45.0 KeV. Here we used a higher beam drift energy to allow a faster diffusion of the beam into the background to avoid making long computer runs. In order to see the effect of the ring on the energy per eigenmode of the various wave modes, we then performed a simulation without the ring being present, but with exactly the same initial conditions as the one with the ring present.

We analyzed the energy per mode of many modes as a function of time to see their time evolution; i.e., we plotted $B^2(k_x, k_y)/2$. Figures 17 and 18 show such results for two modes with and without the ring present. These plots are two of the many which show the energy per mode with the ring present to be roughly an order of magnitude greater than those without the ring. They also show that the lower wave number modes (e.g., $(k_x = 0, k_y = 1)$ shown here), in general, more strongly excited. The plots of Fig. 18 also

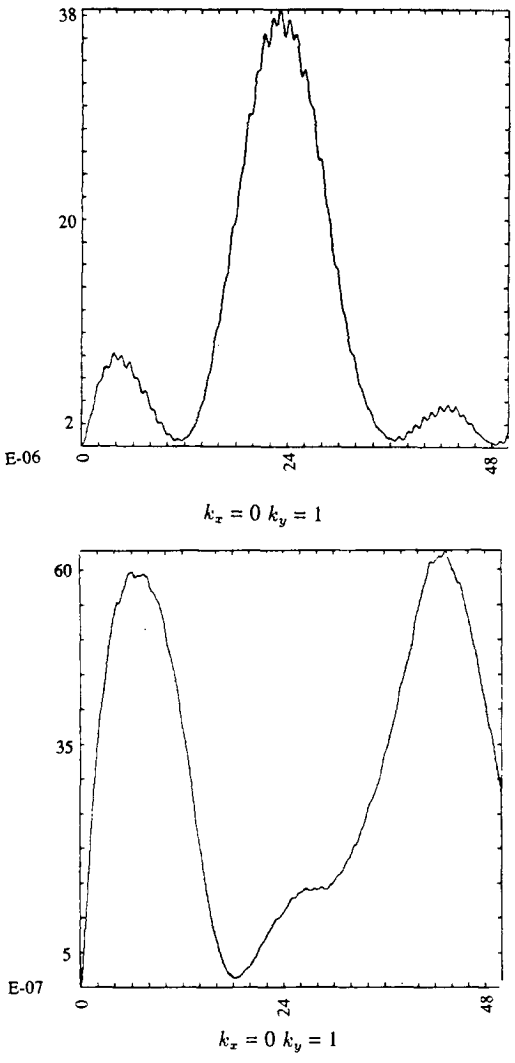

FIG. 17. (Top) Time evolution of the $B^2(k_x = 0, k_y = 1)/2$ for the ring run. (Bottom) Same as the top, but without the ring. Note the difference in scales.

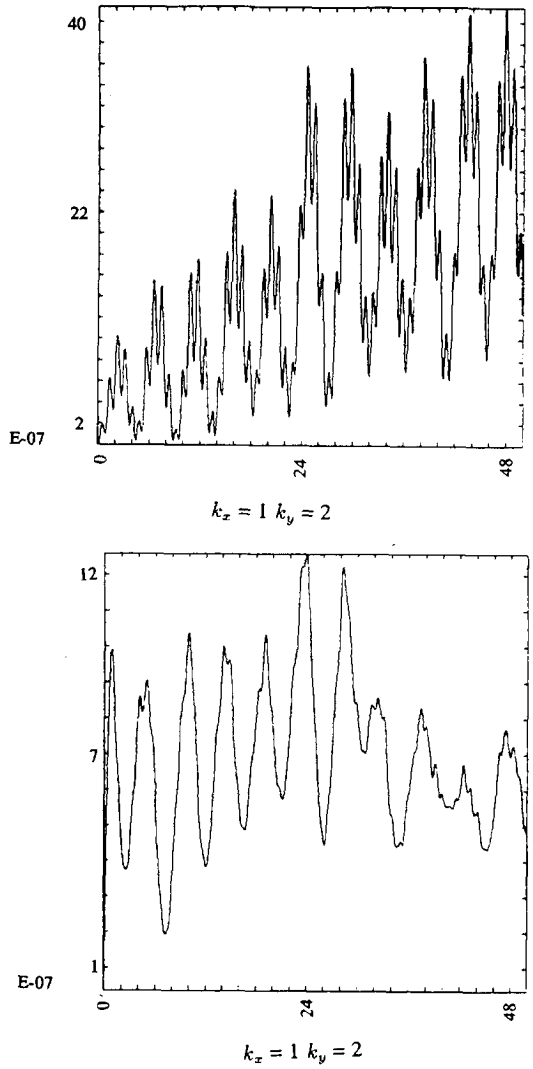

FIG. 18. (Top) Time evolution of the $B^2(k_x = 1, k_y = 2)/2$ for the ring run. (Bottom) Same as the top, but without the ring. Note the difference in scales.

show that even though the higher wave number modes have less energy, their peaks correspond roughly to the $\omega = \omega_{ci}$ harmonic, because given $\omega_{ci} = 6.87$ in this simulation, $\tau_{ci} = 0.91$ which implies that the simulation time of 50, shown on the plots, should contain roughly 55 proton gyroperiods; there are 57 peaks in the plots of Fig. 18. Next Fig. 19 shows a typical power spectra for the ring simulation. There are fairly sharp peaks at $\omega = \omega_{ci}$ and $\omega = 2\omega_{ci}$ in these plots for $\omega_{ci} = 6.87$.

Finally, Fig. 21 shows the dispersion relation corresponding to the lower pictures in Figs. 17 and 18; i.e., the pure thermal runs of this section. This should be contrasted with Fig. 13 in which no low frequency branch in which $\omega \to 0$ as $k_\perp \to 0$ was observed. As mentioned before, we expect the low frequency branch will show Landau damping in that case, while here this is not so, since the Alfven speed is much greater than the ions' thermal speed. Furthermore, another glance at Figs. 17 and 18 reveals the presence of envelopes with frequencies in the lower hybrid ($\omega \simeq kc_A$) range with the carrier frequency at $\omega = \omega_{ci}$. The presence of the peaks at $\omega = \omega_{ci}$ are, of course, more pronounced when the ring is present. The envelopes, being of a lower frequency than the carrier, further testify to the survival of the lower frequency branches and a lack of any Landau Like damping for the JET parameters.

As a next example we simulated the more realistic case in which the background plasma was composed of the deuterium or D^+ and the beam was composed of the

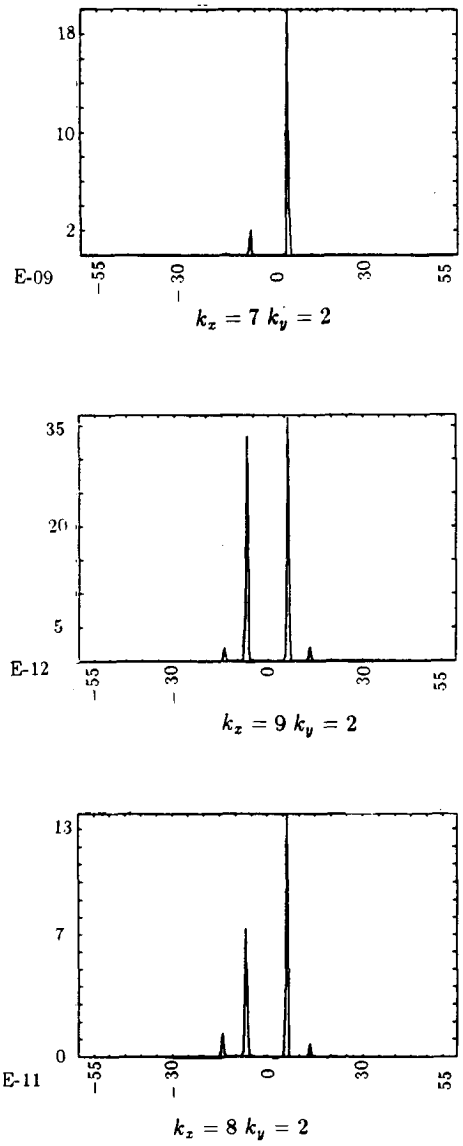

FIG. 19. The power spectra of the B_z component for the ring run.

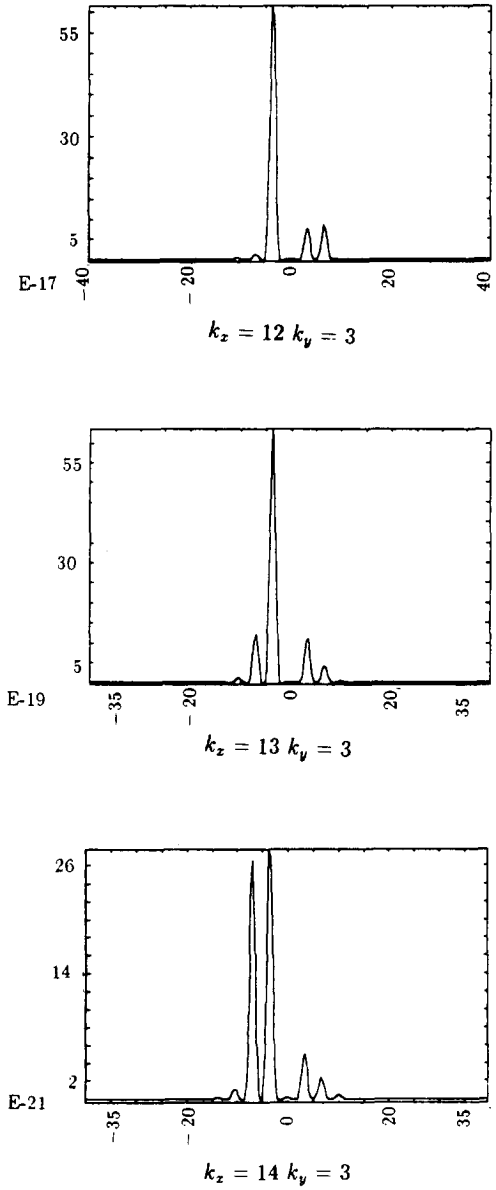

FIG. 20. The power spectra of the B_z component for the 16% H^+ and 84% D^+, with $\omega_{ci} = 6.8$ and $\omega_{cd} = 3.4$.

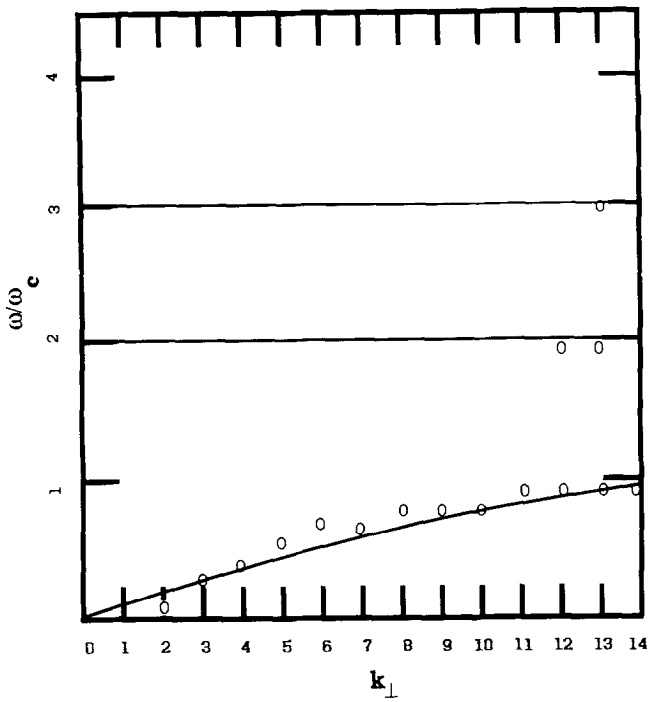

FIG. 21. Dispersion relation of the thermal simulation of the D^+ plasma: o, simulation results; ———, analytic results.

hydrogen ions H^+; the beam composed 16% of the whole plasma.[5] Figure 20 shows typical power spectra for that simulation. Here $\omega_{ci} = 6.87$ corresponds to protons while $\omega_{cd} = \frac{1}{2}\omega_{ci} \cong 3.4$ is the deuterium cyclotron frequency. Thus the peaks at $\omega = 3.4$ must come from the deuterium species in the plasma. This can in fact be the main reason for the observation of the half-harmonic peaks as recorded by the Cottrell *et al.* [12]. The peaks at 6.8 can be a combination of the second harmonic of D^+ and the fundamental of H^+.

3.2. *Simulation of the Fusion Product Experiments*

In this subsection we report simulations of energetic fusion products in a deuterium background. The case that we simulated corresponded to a JET experiment in which the D^+ temperature was 10 KeV and they comprised 99.9% of the plasma. Protons which comprised only 0.1% of the plasma, corresponding to the fusion products, we took their energy to be 1 MeV in the perpendicular direction and 0.1 MeV in the parallel direction; i.e., $(T_p)_\perp =$ 1 MeV and $(T_p)_{||} = 0.1$ MeV. The Alfven speed was 10^7 m/s as before, while the speed of the 1 MeV protons is roughly 9.78×10^6 m/s. The proton gyrofrequency $\omega_{ci} = 10.92$ in the simulations.

In this case we did not use a ring in velocity space as we had done in the previous subsection, but rather we just allowed 0.1% of the particles in the simulation to have the temperatures corresponding to those listed above for the H^+ and have the proton charge to mass ratio, while the rest of the particles in the simulations have their temperatures corresponding to that of the D^+ with its corresponding charge to mass ratio of one-half. The power spectra shown in Fig. 22 correspond to these simulations. There are clear and sharp peaks at $\omega = n\omega_{cd}$ ($\omega_{cd} = 5.46$ is the D^+ gyrofrequency) in confirmation of the conjecture that the free energy available from the fusion products is one possible driver of those modes. Finally, Fig. 23 corresponds to simulations of a case in which the initial magnetic field was not homogeneous but had a linear profile along the x axis; i.e., $\mathbf{B}_{0I} = \mathbf{B}_0((L-x)/L)$, where x is just the distance from the

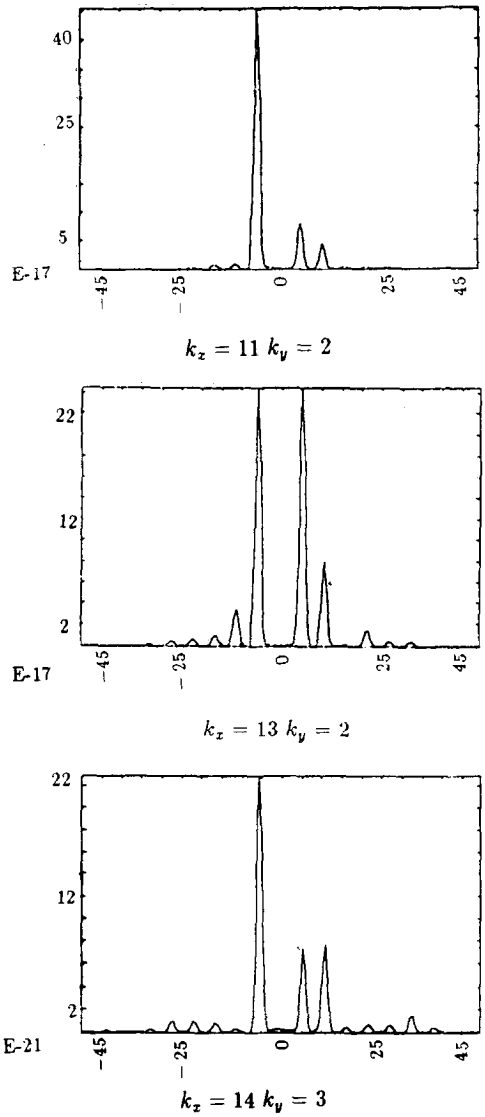

FIG. 22. The power spectra of the B_z component for the fusion product run with $\omega_{cd} = 5.46$, $\omega_{ci} = 10.92$.

[5] All the percentages in this paper correspond to the particle number percentages.

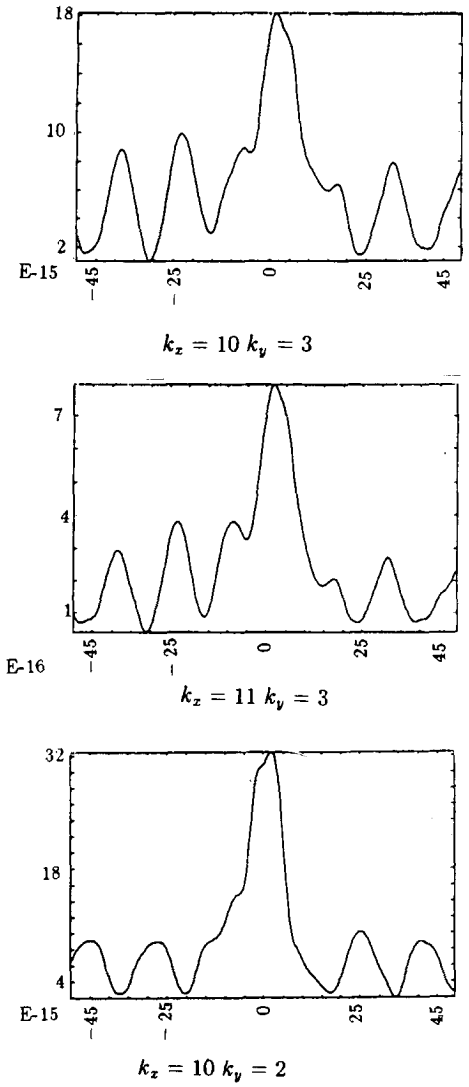

FIG. 23. The power spectra of the B_z component for the fusion product run with the inhomogeneous magnetic field centered at $\omega_{cd} = 5.46$.

left boundary of the simulation box and L is the horizontal length of the simulation box (this models a toroidal magnetic field with L as the major radius of the torus for a large aspect ratio tokamak).[6] Figure 23 gives the power spectra corresponding to that case; there are peaks at roughly $\omega = n\omega_{cd}$ (n = integer) for the inhomogeneous initial magnetic field profile even though we do not have a unique ω_{cd} or ω_{ci}.

CONCLUSION

In this paper the model has undergone a great deal of evolution from that first constructed by Leboeuf *et al.* [1]; in particular, it was generalized to a fully kinetic treatment of the ions; use of an extension of the Richardson extrapolation method for ordinary differential equations was introduced for the particle push and found to improve energy conservation and allow larger time steps. Such revisions of the model proved vital in extension of the model to the applications involving finite Larmor radius effects. In the case of the simulation of the JET experiment, we would not have been able to obtain ion Bernstein waves without the use of the kinetic version of the model. The obtaining of sharp spectral peaks required long runs (e.g., 50 proton gyroperiods on average) for which the large time steps allowed by the Richardson technique were necessary.

Another unique feature of the model is its ability to predict so many different types of wave modes; the kinetic version added ion Bernstein waves to the already existing list of the waves which were predicted by the model. Since waves are so fundamental to understanding plasmas, any code which enables one to study so many different kinds of waves is indeed of great value.

In conclusion the added physics that the model contains should give improvements over the results of MHD codes which are now generally used in space and fusion research.

[6] In the actual experiment the magnetic field profile had hyperbolic dependence on position; i.e., $B_{0I} = B_0/x$ but our code became numerically unstable for such a profile.

APPENDIX A: DERIVATION OF THE DISPERSION RELATION

In this appendix we derive the dispersion relation for the perpendicularly propagating waves, i.e., Eq. (42). The starting equation will be Eq. (41); i.e.,

$$1 = \int_{-\infty}^{+\infty} dv_{\parallel} \int_0^{\infty} v^2\, dv \times \int_0^{2\pi} d\theta \int_{-\infty}^{\theta} d\theta'\, e^{iv(\theta-\theta') - i\kappa(\sin\theta - \sin\theta')} \frac{\partial f_{i0}}{\partial v} \times \cos\theta \left[\frac{ik_x^2 c_A^2}{\omega\omega_c} \cos\theta' + \sin\theta' \right]. \tag{58}$$

This equation can then be cast in the form

$$1 = \int_{-\infty}^{+\infty} dv_{\parallel} \int_0^{\infty} v^2\, dv \frac{\partial f_{i0}}{\partial v} \left(\frac{ik_x^2 c_A^2}{\omega\omega_c} I_1 + I_2 \right), \tag{59}$$

where I_1 and I_2 are defined to be the following integral equations:

$$I_1 = \int_0^{2\pi} d\theta \int_{-\infty}^{\theta} d\theta' \cos\theta \cos\theta'\, e^{i(\theta-\theta') - i\kappa(\sin\theta - \sin\theta')} \tag{60}$$

$$I_2 = \int_0^{2\pi} d\theta \int_{-\infty}^{\theta} d\theta' \cos\theta \sin\theta'\, e^{iv(\theta-\theta') - i\kappa(\sin\theta - \sin\theta')}. \tag{61}$$

We next evaluate I_1 and I_2 as follows.

Let us define $\phi = \theta - \theta'$. Then Eq. (60) will reduce to the equation:

$$I_1 = \int_0^{2\pi} d\theta \cos\theta \int_0^{\infty} d\phi \cos(\theta - \phi)\, e^{iv\phi + i\kappa(\sin(\theta-\phi) - \sin\theta)}. \tag{62}$$

We know that for any function $h(\phi)$ such that $h(\phi) = h(\phi + 2\pi)$ (e.g., periodic in ϕ) the following important property holds, i.e.,

$$\int_0^{\infty} d\phi\, e^{iv\phi} h(\phi) = \sum_{n=0}^{\infty} \int_{2\pi n}^{2\pi(n+1)} d\phi\, e^{iv\phi} h(\phi). \tag{63}$$

Next, by letting $\phi' = \phi - 2\pi n$, Eq. (63) will reduce to

$$\int_0^{\infty} d\phi\, e^{iv\phi} h(\phi) = Q(v) \int_0^{2\pi} d\phi'\, e^{iv\phi'} h(\phi'), \tag{64}$$

where

$$Q(v) = \sum_{n=0}^{\infty} e^{iv2\pi n}. \tag{65}$$

Consequently, I_1 reduces to

$$I_1 = Q(v) \int_0^{2\pi} d\theta \cos\theta \times \int_0^{2\pi} d\phi \cos(\theta - \phi)\, e^{iv\phi + i\kappa(\sin(\theta-\phi) - \sin\theta)}. \tag{66}$$

Next, please note that

$$\cos(\theta - \phi)\, e^{iv\phi + i\kappa\sin(\theta-\phi)} = \left(\frac{i}{\kappa}\frac{\partial}{\partial\phi} + \frac{v}{\kappa}\right) e^{iv\phi + i\kappa\sin(\theta-\phi)}. \tag{67}$$

With this identity then I_1 becomes

$$I_1 = Q(v) \int_0^{2\pi} d\theta \cos\theta \int_0^{2\pi} d\phi\, e^{-i\kappa\sin\theta} \times \left(\frac{i}{\kappa}\frac{\partial}{\partial\phi} + \frac{v}{\kappa}\right) e^{iv\phi + i\kappa\sin(\theta-\phi)}. \tag{68}$$

At this point we need to use the Bessel function identities in order to convert $e^{i\kappa\sin(\theta-\phi)}$ to a form which will make it integrable. The Bessel functions are defined as the coefficients of t^n in the Laurent series expansion of $G(t, z)$, defined as

$$G(t, z) = e^{[z(t - 1/t)/2]} = \sum_{-\infty}^{+\infty} t^n J_n(z), \tag{69}$$

where z is complex. With $t = e^{i\theta}$ this becomes

$$e^{iz\sin\theta} = \sum_{n=-\infty}^{+\infty} e^{in\theta} J_n(z) \tag{70}$$

which results in the relationship

$$e^{i\kappa\sin(\theta-\phi)} = \sum_{n=-\infty}^{\infty} e^{in(\theta-\phi)} J_n(\kappa). \tag{71}$$

Using this identity, along with $\cos\theta = (e^{i\theta} + e^{-i\theta})/2$ in Eq. (68) gives the relationship for I_1,

$$I_1 = \frac{Q(v)}{2} \int_0^{2\pi} d\phi \left(\frac{i}{\kappa}\frac{\partial}{\partial\phi} + \frac{v}{\kappa}\right) e^{iv\phi} \times \int_0^{2\pi} d\theta \sum_{m=-\infty}^{\infty} \sum_{n=-\infty}^{\infty} (e^{i(1-m+n)\theta} + e^{i(-1-m+n)\theta}) \times e^{-in\phi} J_m(\kappa)\, J_n(\kappa). \tag{72}$$

Using the trigonometric identities we can perform the θ integrations, i.e., using

$$\int_0^{2\pi} d\theta\, e^{i\theta(n+1-m)} = 2\pi\delta_{n+1,m} \tag{73}$$

$$\int_0^{2\pi} d\theta\, e^{i\theta(n-m-1)} = 2\pi\delta_{n,m+1}, \tag{74}$$

then I_1 from Eq. (72) reduces to

$$I_1 = \pi Q(v) \int_0^{2\pi} d\phi \left(\frac{i}{\kappa}\frac{\partial}{\partial\phi} + \frac{v}{\kappa}\right) \times \left(\sum_{n=-\infty}^{\infty} e^{i(v-n)\phi} + e^{i(v-n-1)\phi}\right) J_n(\kappa)\, J_{n+1}(\kappa). \tag{75}$$

Upon applying $((i/\kappa)(\partial/\partial\phi) + v/\kappa)$ inside this integral and carrying out the ϕ integrations (after some algebraic manipulations), I_1 becomes

$$I_1 = \pi Q(v) \left\{ \sum_{n=-\infty}^{\infty} \left(\frac{n}{\kappa}\frac{e^{iv2\pi} - 1}{i(v-n)} + \frac{n+1}{\kappa}\frac{e^{iv2\pi} - 1}{i(v-n-1)}\right) \times J_n(\kappa)\, J_{n+1}(\kappa) \right\}. \tag{76}$$

Using the fact that $|e^{i2\pi v}| < 1$ for $\mathrm{re}(iv) = -\omega_I/\omega_c < 0$, we conclude that $Q(v)$ from Eq. (65) is simply a geometric series which can be cast in the form

$$Q(v) = \sum_{n=0}^{\infty} e^{iv2\pi n} = \frac{1}{1 - e^{i2\pi v}}. \tag{77}$$

Using this identity for $Q(v)$ in Eq. (76) finally results in the identity for I_1,

$$I_1(\kappa, v) = \frac{\pi i}{\kappa} \sum_{-\infty}^{\infty} \left(\frac{2nv - 2n^2 - 2n + v}{(v-n)(v-n-1)} \right) \times J_n(\kappa)\, J_{n+1}(\kappa). \tag{78}$$

We now turn to $I_2(\kappa, v)$. Recall from Eq. (61) that

$$I_2 = \int_0^{2\pi} d\theta \int_{-\infty}^{\theta} d\theta' \cos\theta \sin\theta' \, e^{iv(\theta-\theta') - i\kappa(\sin\theta - \sin\theta')}. \tag{79}$$

The only difference between this and I_1 is in the presence of the $\sin\theta'$ in the integrand. By exactly following the same steps as we did for I_1, we arrive at

$$I_2(\kappa, v) = \frac{\pi}{2} \sum_{-\infty}^{+\infty} \left(\frac{[J_m(\kappa)]^2}{v-1-m} - \frac{[J_m(\kappa)]^2}{v-m+1} \right). \tag{80}$$

Now that we have I_1 and I_2, after substituting them in Eq. (59) using $v = \omega/\omega_c$ and $\kappa = k_x v/\omega_c$, for a background Maxwellian distribution function, $f_{i0} = (1/\pi^{3/2} a_{||} a_\perp^2)\, e^{-v_{||}^2/a_{||}^2 - v_\perp^2/a_\perp^2}$, we finally obtain the analytic dispersion relation (we let $k_x \to k_\perp$ without loss of generality):

$$1 + \int_0^{+\infty} v^2\, dv \left[-2 \frac{v e^{-v^2/a_\perp^2}}{\pi a_\perp^4} \right] \times \left\{ \left(\frac{k_\perp c_A^2 \pi}{\omega v} \right) \times \left(\sum_{n=-\infty}^{+\infty} \left[\frac{[(2n+1)\omega - 2n(n+1)\,\omega_c]\,\omega_c}{(\omega - n\omega_c)(\omega - (n+1)\,\omega_c)} \times J_n\left(\frac{k_\perp v}{\omega_c}\right) J_{n+1}\left(\frac{k_\perp v}{\omega_c}\right) \right] \right) + \sum_{n=-\infty}^{+\infty} \frac{\pi}{2} \times \left[\frac{[J_n(k_\perp v/\omega_c)]^2}{\omega + (1-n)\,\omega_c} - \frac{[J_n(k_\perp v/\omega_c)]^2}{\omega - (1+n)\,\omega_c} \right] \right\} = 0. \tag{81}$$

APPENDIX B: THE ERROR DEPENDENCE OF $\mathbf{v}_i$ ON THE TIME STEP Δt

In this appendix we give a plausible proof of the $(\Delta t)^2$-dependence of the error in $\mathbf{v}_i$, introduced upon the finite differencing operations in the Vlasov ion zero mass electron model. The starting equations will be the push equations for the velocity. Recall from Table I that steps (3) and (7) were those of the velocity push in a given time step. Those two steps are the following respectively:

$$\mathbf{v}^l = \mathbf{v}^{l-1/2} + (\mathbf{v}^{l-1/2} - \mathbf{v}'^{l-1/2}) \times \mathbf{B}^l\, \Delta t/2 + \mathbf{F}_B^l\, \Delta t/2 \tag{82}$$

$$\mathbf{v}^{l+1/2} = \mathbf{v}^l + (\mathbf{v}^l - \mathbf{v}'^l) \times \mathbf{B}^l\, \Delta t/2 + \mathbf{F}_B^l\, \Delta t/2. \tag{83}$$

Combining these two steps gives the following result for the advancement of the velocity for one full time step from $l-\frac{1}{2}$ to $l+\frac{1}{2}$:

$$\mathbf{v}^{l+1/2} = \mathbf{v}^{l-1/2} + [(\mathbf{v}^{l-1/2} - \mathbf{v}'^{l-1/2}) + (\mathbf{v}^l - \mathbf{v}'^l)] \times \mathbf{B}^l\, \Delta t/2 + \mathbf{F}_B^l\, \Delta t. \tag{84}$$

Here $\mathbf{F}_B^l$ is simply the Maxwell stress tensor defined to be

$$\mathbf{F}_B^l = \frac{n_0}{n^l} \left[-\nabla \cdot \left(\frac{B^2}{2} \overline{\overline{\mathbb{I}}} - \mathbf{BB} \right) \right]^l. \tag{85}$$

The method that we shall use in determining the error upon finite differencing will be the following: We use the velocity advancement Eq. (84) once with a time step $\Delta t_1 = 2\Delta t$ and advance $\mathbf{v}_i$ from $l-\frac{1}{2}$ to $l+\frac{3}{2}$; then we use Eq. (84) twice in sequence with the time step Δt to achieve the same goal. We subtract the two results and determine the error by observing the dependence of that difference on Δt and the initial conditions at $l-\frac{1}{2}$. We must remember that the corresponding time step for position-dependent quantities is the time step l in Eq. (84), e.g., $\mathbf{B}$ and the Maxwell stress tensor.

So let us use Eq. (84) with $\Delta t_1 = 2\Delta t$ to advance $\mathbf{v}^{l-1/2}$ to $\tilde{\mathbf{v}}^{l+3/2}$. We note that for $\Delta t_1 = 2\Delta t$, one full time step advancement corresponds to two for the case of using Δt. Consequently, as one goes from $(l-\frac{1}{2})\,\Delta t$ to $(l+\frac{3}{2})\,\Delta t$, the middle time is simply $(l+\frac{1}{2})\,\Delta t$ rather than $l\,\Delta t$. With this in mind then Eq. (84) gives

$$\tilde{\mathbf{v}}^{l+3/2} = \mathbf{v}^{l-1/2} + [(\mathbf{v}^{l-1/2} - \mathbf{v}'^{l-1/2}) + (\mathbf{v}^{l+1/2} - \mathbf{v}'^{l+1/2})] \times \mathbf{B}^{l+1/2}\, \Delta t + \mathbf{F}_B^{l+1/2} 2\, \Delta t. \tag{86}$$

Clearly, advancing $\mathbf{v}^{l+1/2}$ obtained from Eq. (84) one more time step Δt will advance it to the time $(l+3/2)\,\Delta t$; this gives

$$\mathbf{v}^{l+3/2} = \mathbf{v}^{l-1/2} + [\mathbf{v}^{l-1/2} - \mathbf{v}'^{l-1/2} + \mathbf{v}^l - \mathbf{v}'^l] \times \mathbf{B}^l\, \Delta t/2 + \mathbf{F}_B^l\, \Delta t + [\mathbf{v}^{l+1/2} - \mathbf{v}'^{l+1/2} + \mathbf{v}^{l+1} - \mathbf{v}'^{l+1}] \times \mathbf{B}^{l+1}\, \Delta t/2 + \mathbf{F}_B^{l+1}\, \Delta t. \tag{87}$$

Subtracting Eq. (87) from Eq. (86) gives

$$\mathbf{v}^{l+3/2} - \tilde{\mathbf{v}}^{l+3/2} = [\mathbf{v}^{l-1/2} - \mathbf{v}'^{l-1/2} + \mathbf{v}^l - \mathbf{v}'^l] \times \mathbf{B}^l\, \Delta t/2 + \mathbf{F}_B^l\, \Delta t + [\mathbf{v}^{l+1/2} - \mathbf{v}'^{l+1/2} + \mathbf{v}^{l+1} - \mathbf{v}'^{l+1}] \times \mathbf{B}^{l+1}\, \Delta t/2 + \mathbf{F}_B^{l+1}\, \Delta t - [\mathbf{v}^{l-1/2} - \mathbf{v}'^{l-1/2} + \mathbf{v}^{l+1/2} - \mathbf{v}'^{l+1/2}] \times \mathbf{B}^{l+1/2}\, \Delta t - 2\mathbf{F}_B^{l+1/2}\, \Delta t. \tag{88}$$

As mentioned earlier, we shall attempt to write everything on the right-hand side of Eq. (88) in terms of the quantities at the starting time, which in this case is $(l-1/2)\,\Delta t$ for the velocity and $l\,\Delta t$ for the position-dependent quantities. For that we again go back to the Table I. We immediately observe from items (5) and (10) that

$$\begin{aligned}\mathbf{B}^{l+1/2} &= \langle \mathbf{B}\rangle^l + \mathscr{F}(\mathbf{v}^l, \mathbf{B}^l, n^l)\,\Delta t/2 \\ &= \langle \mathbf{B}\rangle^l + O(\Delta t) \qquad (89)\\ \mathbf{B}^{l+1} &= \mathbf{B}^l + \mathscr{F}(\mathbf{v}^{l+1/2}, \mathbf{B}^{l+1/2}, n^{l+1/2})\,\Delta t \\ &= \mathbf{B}^l + O(\Delta t). \qquad (90)\end{aligned}$$

Here $\mathscr{F}$ is just the right-hand side of Faraday's law. Clearly, the second terms on the right-hand sides of Eqs. (89) and (90) give rise to terms of order $(\Delta t)^2$ and higher when substituted in Eq. (88), so we only need to consider the first terms of these equations. However, there appears $\langle \mathbf{B}\rangle^l$ which is not exactly the same as $\mathbf{B}^l$, and that could complicate our analysis somewhat. We can argue that the act of smoothing of the magnetic field could have made those quantities very close to each other, since very short wavelength disturbances are eliminated by such an operation and thus large variations within a grid distance are avoided. As a result, for this analysis one can take $\langle \mathbf{B}\rangle^l$ and $\mathbf{B}^l$ to be the same. Thus the first part of Eq. (88) which could have a weaker than quadratic dependence on Δt will be those terms proportional to $\mathbf{B}^l\,\Delta t$, while the second part is that which is proportional to the Maxwell stress tensor $\mathbf{F}_B$; we discuss these terms next.

The part which is proportional to $\mathbf{B}^l\Delta t$ is:

$$\begin{aligned}&\{\tfrac{1}{2}[\mathbf{v}^{l-1/2} - \mathbf{v}'^{l-1/2} + \mathbf{v}^l - \mathbf{v}'^l] \\ &\quad + \tfrac{1}{2}[\mathbf{v}^{l+1/2} - \mathbf{v}'^{l+1/2} + \mathbf{v}^{l+1} - \mathbf{v}'^{l+1}] \\ &\quad - [\mathbf{v}^{l-1/2} - \mathbf{v}'^{l-1/2} + \mathbf{v}^{l+1/2} - \mathbf{v}'^{l+1/2}]\} \times \mathbf{B}^l\,\Delta t \\ &= \tfrac{1}{2}\{(\mathbf{v}^l - \mathbf{v}^{l-1/2}) - (\mathbf{v}'^l - \mathbf{v}'^{l-1/2}) \\ &\quad + (\mathbf{v}^{l+1} - \mathbf{v}^{l+1/2}) - (\mathbf{v}'^{l+1} - \mathbf{v}'^{l+1/2})\} \times \mathbf{B}^l\,\Delta t. \qquad (91)\end{aligned}$$

Clearly, since the last two parenthesis in Eq. (91) involve quantities at the times $(l+\frac{1}{2})\,\Delta t$ and $(l+1)\,\Delta t$, thus when they are written in terms of their respective values at $(l-\frac{1}{2})\,\Delta t$, they will involve terms of the $O(\Delta t)$ or higher and therefore contribute to quadratic or higher order dependence on Δt. The first parenthesis $(\mathbf{v}^l - \mathbf{v}^{l-1/2})$, on the other hand, according to Eq. (82) when written in terms of $(l-\frac{1}{2})$-dependent velocities and the l-dependent Maxwell stress tensor will have a Δt dependence and will thus contribute to a quadratic dependence on Δt. The same argument goes for the second parenthesis in Eq. (91), since $\mathbf{v}'$ is obtained from $\mathbf{v}$ by interpolation and should have the same Δt dependence. As a result, the part which is proportional to

Finally, we examine the part which is proportional to the Maxwell stress tensor, i.e.,

$$\begin{aligned}&\mathbf{F}_B^l\,\Delta t + \mathbf{F}_B^{l+1}\,\Delta t - 2\mathbf{F}_B^{l+1/2}\,\Delta t \\ &\quad = \left\{\frac{n_0}{n^l}\left[-\nabla\cdot\left(\frac{B^2}{2}\,\underline{\underline{\mathrm{I}}} - \mathbf{BB}\right)\right]^l\right. \\ &\quad\quad + \frac{n_0}{n^{l+1}}\left[-\nabla\cdot\left(\frac{B^2}{2}\,\underline{\underline{\mathrm{I}}} - \mathbf{BB}\right)\right]^{l+1} \\ &\quad\quad \left. - 2\,\frac{n_0}{n^{l+1/2}}\left[-\nabla\cdot\left(\frac{B^2}{2}\,\underline{\underline{\mathrm{I}}} - \mathbf{BB}\right)\right]^{l+1/2}\right\}\Delta t. \qquad (92)\end{aligned}$$

In this equation the only term which can have a Δt dependence rather than a $(\Delta t)^2$ dependence is that which depends only on $\mathbf{B}^l$. After using finite differences for writing $\mathbf{B}^{l+1/2}$ and $\mathbf{B}^{l+1}$ in terms of $\mathbf{B}^l$ in the second and the third brackets of Eq. (92) we obtain

$$\begin{aligned}&\left(\frac{n_0}{n^l} + \frac{n_0}{n^{l+1}} - 2\,\frac{n_0}{n^{l+1/2}}\right)\left[-\nabla\cdot\left(\frac{B^2}{2}\,\underline{\underline{\mathrm{I}}} - \mathbf{BB}\right)\right]^l \Delta t \\ &\quad = n_0\left(\frac{n^{l+1}(n^{l+1/2} - n^l) + n^l(n^{l+1/2} - n^{l+1})}{n^l n^{l+1} n^{l+1/2}}\right) \\ &\quad\quad \times\left[-\nabla\cdot\left(\frac{B^2}{2}\,\underline{\underline{\mathrm{I}}} - \mathbf{BB}\right)\right]^l \Delta t. \qquad (93)\end{aligned}$$

Recall that the densities are obtained from the particle positions by aerea weighting interpolation [3, 4]. For example, the density at a given fixed grid location $\mathbf{x}_j$ at a time $t = l\,\Delta t$ is obtained by the weighting scheme,

$$n^l(\mathbf{x}_j) = \sum_{i\in\Delta_j} w(\mathbf{x}_i(l\,\Delta t), \mathbf{x}_j) = \sum_{i\in\Delta_j} w^l(\mathbf{x}_i(t), \mathbf{x}_j), \qquad (94)$$

where $t = l\,\Delta t$ is the reference time, and the index i refers to particles, while j refers to grid locations.

Clearly then, upon using a Taylor expansion, one can estimate $n^{l+1/2}$ and n^{l+1} from this equation as follows:

$$\begin{aligned}n^{l+1/2}(\mathbf{x}_j) &= \sum_{i\in\Delta_j} w\left(\mathbf{x}_i\left(t + \frac{\Delta t}{2}\right), \mathbf{x}_j\right) \\ &= \sum_{i\in\Delta_j}\left(w(\mathbf{x}_i(t), \mathbf{x}_j) + \left(\frac{\partial w}{\partial \mathbf{x}_i}\,\frac{\partial \mathbf{x}_i}{\partial t}\right)_{t=l\,\Delta t}\left(\frac{\Delta t}{2}\right)\right) \\ &= n^l(\mathbf{x}_j) + \sum_{i\in\Delta_j}\left(\frac{\partial w^l}{\partial \mathbf{x}_i}\cdot\mathbf{v}_i\right)\frac{\Delta t}{2}. \qquad (95)\end{aligned}$$

Likewise,

$$n^{l+1}(\mathbf{x}_j) = n^l(\mathbf{x}_j) + \sum_{i\in\Delta_j}\left(\frac{\partial w^l}{\partial \mathbf{x}_i}\cdot\mathbf{v}_i\right)\Delta t. \qquad (96)$$

Clearly then, the two parenthesis which appear on the right-